PROCEEDINGS OF
THE ROYAL SOCIETY A
MATHEMATICAL, PHYSICAL AND ENGINEERING SCIENCES

Linear analysis of ice-shelf topography response to basal melting and freezing

Journal:	*Proceedings A*
Manuscript ID	RSPA-2023-0290.R2
Article Type:	Research
Date Submitted by the Author:	n/a
Complete List of Authors:	Stubblefield, Aaron; Dartmouth College, Thayer School of Engineering Wearing, Martin; The University of Edinburgh School of GeoSciences Meyer, Colin; Dartmouth College, Thayer School of Engineering
Subject:	Glaciology < EARTH SCIENCES, Mathematical modelling < MATHEMATICS, Geophysics < EARTH SCIENCES
Keywords:	ice-shelf melting, ice-shelf freeze-on, ice-shelf channels, floating viscous sheets, topographic relaxation
Subject Category:	Earth Science
Note: The following files were submitted by the author for peer review, but cannot be converted to PDF. You must view these files (e.g. movies) online.	
latex-files.zip	

Author-supplied statements

Relevant information will appear here if provided.

Ethics

Does your article include research that required ethical approval or permits?:
This article does not present research with ethical considerations

Statement (if applicable):
CUST_IF_YES_ETHICS :No data available.

Data

It is a condition of publication that data, code and materials supporting your paper are made publicly available. Does your paper present new data?:
Yes

Statement (if applicable):
The following data availability statement is provided in the attached main document:
No new data are presented in this study. The code is openly available at https://www.doi.org/10.5281/zenodo.8171998 (DOI: 10.5281/zenodo.8171998).

Conflict of interest

I/We declare we have no competing interests

Statement (if applicable):
CUST_STATE_CONFLICT :No data available.

PROCEEDINGS A

royalsocietypublishing.org/journal/rspa

Research

Check for updates

Article submitted to journal

Subject Areas:
glaciology, geophysics, mathematical modeling

Keywords:
ice-shelf melting, ice-shelf freeze-on, ice-shelf channels, floating viscous sheets, topographic relaxation

Author for correspondence:
A. G. Stubblefield
e-mail:
aaron.g.stubblefield@dartmouth.edu

Linear analysis of ice-shelf topography response to basal melting and freezing

A. G. Stubblefield[1], M. G. Wearing[2] and C. R. Meyer[1]

[1]Thayer School of Engineering, Dartmouth College, Hanover, NH, USA
[2]School of Geosciences, University of Edinburgh, Edinburgh, UK

Floating ice shelves in Antarctica and Greenland limit land-ice contributions to sea level rise by resisting the flow of grounded ice. Melting at the surface and base of ice shelves can lead to destabilisation by promoting thinning and fracturing. Basal melting often results in channelised features that manifest as surface topography due to buoyancy. The assumption of hydrostatic flotation commonly underlies estimates of basal melting rates. However, numerical simulations and ice-penetrating radar data have shown that narrow topographic features do not necessarily satisfy the local flotation condition. Here, we introduce a linearised model for ice-shelf topographic response to basal melting perturbations to quantify deviations from hydrostatic flotation and the stability of topography. While hydrostatic flotation is the dominant behaviour at wavelengths greater than the ice thickness, ice elevation can deviate from the perfect flotation condition at smaller wavelengths. The linearised analysis shows that channelised features can be stable when the timescale of extensional thinning is small relative to the timescale of viscous flow towards the channel. When extension is non-negligible, channels can break through the ice column. We validate the linearised analysis by comparing numerical solutions to a nonlinear ice-flow model with steady-state solutions obtained via a Green's function.

THE ROYAL SOCIETY PUBLISHING

1. Introduction

Ice shelves and floating ice tongues in Greenland and Antarctica slow ice-mass loss and land-ice contributions to sea level rise by buttressing the flow of grounded ice [1–4]. Subglacial outflow near grounding lines and warm seawater intrusions can cause localised melting at the base of ice shelves [5–8]. Topographic features that are elongated in one direction, commonly called ice-shelf channels, have been found on many ice shelves and arise from localised melting at the base [7,9]. These anomalous topographic features manifest at the ice-shelf surface due to buoyancy. Ice-shelf channels have been associated with a variety of features including rifts, subglacial outflow, persistent polynyas, and terracing of the basal surface [9–11]. While channel formation is driven by persistent plumes of buoyant water, the dynamics vary and are influenced by the plume source (i.e., oceanic or subglacial), the presence of heterogeneous surfaces, and ice deformation [7,12–15].

Although melting dominates the basal mass balance of most Antarctic ice shelves [16], altimetry, ice-penetrating radar, and numerical models have shown that many ice shelves have regions where water is freezing to the base [17–22]. Borehole drilling has shown that thick units of frozen-on marine ice exist beneath the Amery Ice Shelf [23–25] and the Ronne-Filchner Ice Shelf [26,27]. Marine ice can have different rheological properties than meteoric ice due to differences in crystal size and orientation as well as the presence of interstitial brine [28]. Marine ice has also been found within suture zones, boundaries within ice shelves that separate different flow units, and may contribute to the structural stability of ice shelves by impeding fracture propagation [29–33]. For these reasons, quantifying the mechanical effects of marine ice accretion and refining inferences from ice-shelf topography remain important areas of investigation.

The melting or freezing rate at the base of ice shelves can be estimated from surface observations under the assumptions that the ice is undergoing hydrostatic flotation and that the horizontal velocity is depth-independent. In this limit, the surface elevation of the ice shelf relative to sea level only depends on the ice thickness and the densities of ice and water. However, since ice flows like a viscous fluid over long time scales [34–36], deviatoric (bridging) stresses in the ice can lead to a non-hydrostatic state where the ice-surface elevation is diminished relative to the hydrostatic elevation [37–39]. Ice-penetrating radar data from the Fimbul Ice Shelf, East Antarctica, shows that narrow basal channels can be associated with diminished topographic anomalies [14]. Similarly, hydrostatic imbalance was found in the vicinity of a channel on the Getz Ice Shelf, West Antarctica, by comparing hydrostatic flotation thickness estimates with ice thickness obtained from radar profiles along NASA Operation IceBridge transects [40]. When hydrostatic balance is not satisfied exactly, the velocity is not depth-independent due to the presence of a secondary flow that balances the formation of basal channels. Deviation of the surface velocity and elevation from hydrostatic balance produces errors in melting-rate estimates that are based solely on surface observations [39,40].

Previous models of subglacial channels have been used to explore deviations from hydrostatic flotation [38,39], coupling with ocean physics [13,41–43], inclusion of viscoelastic effects [44,45], and evolution of ice-shelf stratigraphy [46]. A small-perturbation approximation of the Stokes equations has been used to model the evolution of crevasses in ice shelves over long time scales in relation to oceanic forcing [47,48]. Similar perturbation models for Newtonian and power-law fluids have been developed in the context of necking during lithospheric extension and folding during compression [49,50]. While detailed analyses of Stokes-based perturbation models have been developed previously for grounded ice [51–54], similar analyses for floating ice shelves have not been developed beyond the crevasse evolution model [47].

Here, we develop a detailed linearised analysis of the ice-shelf topographic response to melting or freezing perturbations at the base. Our focus is on modelling the competition between topographic decay and buoyancy from the basal forcing rather than developing a model for the basal melt rate, which we consider to a be a prescribed field. We derive a linearised model that describes small perturbations to a floating viscous layer undergoing depth-independent extension and advection. We simplify the model and analyse the problem via a spectral decomposition. We

royalsocietypublishing.org/journal/rspa Proc R Soc A 0000000

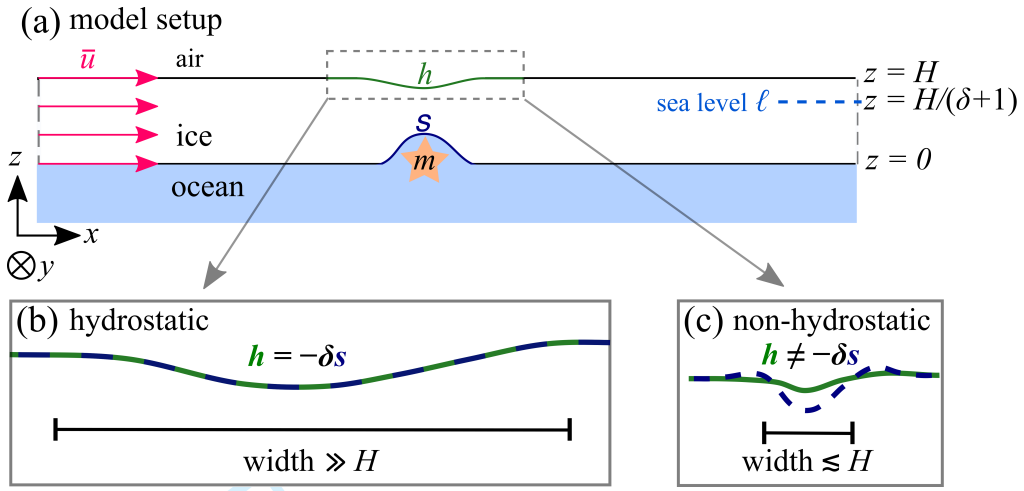

Figure 1. (a) Sketch of model variables. The ice-surface elevation perturbation is h, the elevation perturbation at the ice-water interface is s, the melting rate is m, the ice thickness is H, the sea level is ℓ, the flotation factor is $\delta = \rho_w/\rho_i - 1$, and the background horizontal velocity in the x direction is $\bar{u}$. The y direction is pointing out of the page. (b) Example of a topographic anomaly that is wide relative to the ice thickness and satisfies the perfect flotation condition ($h = -\delta s$) locally. (c) Example of a narrow topographic anomaly that does not satisfy the perfect flotation condition locally.

quantify conditions under which ice-elevation anomalies approach perfect flotation as well as the stability of steady-state solutions for a range of extensional regimes and melting rates. To test the validity of the small-perturbation approach, we compare numerical solutions obtained by solving a fully nonlinear ice-flow problem with a finite element method to semi-analytical steady-state solutions that we obtain with a Green's function. We conclude by discussing implications and avenues for further research.

2. Model derivation

(a) Governing equations

First, we outline a general Stokes model for ice-shelf flow. We assume that the domain is an ice shelf of finite thickness H and infinite horizontal extent (Figure 1a). The domain is defined by $|x| < \infty$, $|y| < \infty$, and $s \leq z \leq h$, where h and s are the upper and lower surfaces of the ice shelf, respectively. We assume that ice deforms according to the incompressible Stokes equations

$$-\boldsymbol{\nabla} p + \boldsymbol{\nabla}\cdot(2\eta\dot{\boldsymbol{\varepsilon}}) = \rho_i \boldsymbol{g} \tag{2.1}$$

$$\boldsymbol{\nabla}\cdot\boldsymbol{u} = 0, \tag{2.2}$$

where $\mathbf{u} = [u, v, w]^T$ is the velocity, $\dot{\boldsymbol{\varepsilon}} = \frac{1}{2}\left(\boldsymbol{\nabla}\boldsymbol{u} + \boldsymbol{\nabla}\boldsymbol{u}^T\right)$ is the strain rate, η is the ice viscosity, p is the pressure, ρ_i is the ice density, and $\boldsymbol{g} = [0, 0, -g]^T$ is gravitational acceleration with magnitude g. For simplicity, we consider a constant (Newtonian) viscosity in the linearised analysis below, but later compare the analytical results to finite element solutions with a shear-thinning (Glen's law) viscosity [34–36].

We assume that the traction vanishes at the upper surface ($z = h$), which is equivalent to

$$[2\eta\dot{\boldsymbol{\varepsilon}} - p\mathbf{I}]\cdot\boldsymbol{n} = \mathbf{0}, \tag{2.3}$$

where $\boldsymbol{n}$ is an upward-pointing unit normal to the ice boundary and $\mathbf{I}$ is the identity tensor. The normal stress at the ice-water interface ($z = s$) equals the water pressure and the shear stress

royalsocietypublishing.org/journal/rspa Proc R Soc A 0000000

vanishes,

$$[2\eta\dot{\boldsymbol{\epsilon}} - p\mathbf{I}] \cdot \boldsymbol{n} = \rho_{\mathrm{w}} g(\ell - s)\boldsymbol{n}, \tag{2.4}$$

where ρ_{w} is the water density and $z = \ell$ is the (far-field) sea level. Below, we set the sea level to $\ell = (\rho_{\mathrm{i}}/\rho_{\mathrm{w}})H$, where H is the ice thickness in the uniform reference state.

The upper and lower surfaces of the ice shelf evolve according to kinematic equations that are coupled to the Stokes flow equations. The upper surface, $z = h(x, y, t)$, evolves according to

$$\frac{\partial h}{\partial t} + u\frac{\partial h}{\partial x} + v\frac{\partial h}{\partial y} = w + a, \tag{2.5}$$

where a denotes accumulation or ablation at the ice-shelf surface. Similarly, the lower surface, $z = s(x, y, t)$, evolves according to

$$\frac{\partial s}{\partial t} + u\frac{\partial s}{\partial x} + v\frac{\partial s}{\partial y} = w + m, \tag{2.6}$$

where m is the basal melting or freezing rate (Figure 1). We also require that all fields approach appropriate far-field reference states in the limits $|x| \to \infty$ and $|y| \to \infty$, which are naturally incorporated in the perturbation-based framework described below. While our focus is on a spectral analysis of the linearised problem, we also compare the results to solutions obtained by solving the fully nonlinear problem (2.1)-(2.6) with a finite element method, subject to a shear-thinning flow law for the viscosity and additional boundary conditions on the side-walls of the computational domain.

(b) Perturbation equations

Next, we derive a linearisation of the problem (2.1)-(2.6). We take perturbations relative to an idealised reference state that is characterised by depth-independent extension and advection, a constant (Newtonian) ice viscosity $\bar{\eta}$, perfect flotation, and no surface accumulation or basal melting (Figure 1). Denoting the reference states with bars, these conditions are given by

$$\begin{aligned} &\bar{u} = \bar{u}_0 + E_{xx}x, \quad \bar{v} = \bar{v}_0 + E_{yy}y, \quad \bar{w} = -E(z - \ell), \quad \bar{p} = \rho_{\mathrm{i}} g(\bar{h} - z) - 2\bar{\eta}E, \\ &\bar{h} = \ell + (H - \ell)e^{-Et}, \quad \bar{s} = \ell(1 - e^{-Et}), \quad \bar{\ell} = \frac{\rho_{\mathrm{i}}}{\rho_{\mathrm{w}}}H, \quad \bar{a} = \bar{m} = 0 \end{aligned} \tag{2.7}$$

where H is the initial ice thickness, E_{xx} and E_{yy} are constant principal strain rates, $E = E_{xx} + E_{yy}$ is the thinning rate, and $\bar{u}_0$ and $\bar{v}_0$ are advective components of the background flow. The advective components can be ignored in the perturbation analysis if the melting perturbation advects with the basal topography or is oriented in the along-flow direction. Thus, the advective components are primarily relevant to flow across a stationary melting source as in, for example, a subglacial outflow plume [9]. While we assume a Newtonian rheology for simplicity, an extensional stress regime with shear-thinning rheology has been analysed previously in a linearised framework [47,50]. In the limit of no extension ($E \to 0$), the cryostatic reference state is comparable to previous work that explored channel evolution and non-hydrostatic stresses with numerical simulations of idealised, laterally confined ice shelves [39]. We will assume throughout that the background thickness remains approximately constant, $\bar{h} - \bar{s} \approx H$, over the timescales considered here because our focus is on small thinning rates. Alternatively, the reference ice thickness also remains constant if the surface accumulation and basal melting rates in the reference state balance the vertical velocity.

We introduce small, localised perturbations (denoted by asterisks) to the reference states via

$$\begin{aligned} &u = \bar{u} + \epsilon u_*, \quad v = \bar{v} + \epsilon v_*, \quad w = \bar{w} + \epsilon w_*, \quad p = \bar{p} + \epsilon p_*, \\ &s = \bar{s} + \epsilon s_*, \quad h = \bar{h} + \epsilon h_*, \quad m = \bar{m} + \epsilon m_*, \end{aligned} \tag{2.8}$$

where ϵ is a small parameter. To facilitate the analysis below, we assume that the perturbations are localised around the extensional axis and, therefore, decay away from the origin. For simplicity,

we do not consider perturbations to the surface accumulation (or ablation) rate. We revisit possible sources of surface-mass balance perturbations and related model extensions in the discussion. Here, we consider the melt-rate perturbation to be a prescribed field and focus on the topographic response to this basal forcing. We revisit the importance of process-based models for channel formation that capture feedbacks between melting and basal topography in the discussion.

We insert the perturbations (2.8) into (2.1)-(2.2) and discard the $O(\epsilon^2)$ terms to obtain a homogeneous, linear Stokes problem for the perturbed fields,

$$-\boldsymbol{\nabla} p_* + \bar{\eta}\nabla^2 \boldsymbol{u}_* = \mathbf{0} \tag{2.9}$$

$$\boldsymbol{\nabla}\cdot \boldsymbol{u}_* = 0. \tag{2.10}$$

Although not explored here, a non-Newtonian reference state results in a perturbed momentum balance that depends on the stress exponent and background principal strain rates [47]. The surface kinematic equations (2.5) and (2.6) reduce to

$$\frac{\partial h_*}{\partial t} + \bar{u}_0 \frac{\partial h_*}{\partial x} + \bar{v}_0 \frac{\partial h_*}{\partial y} = w_* + Eh \tag{2.11}$$

$$\frac{\partial s_*}{\partial t} + \bar{u}_0 \frac{\partial s_*}{\partial x} + \bar{v}_0 \frac{\partial s_*}{\partial y} = w_* + m_* + Es, \tag{2.12}$$

where we have made the approximations

$$E_{xx} x \frac{\partial \zeta}{\partial x} \approx -E_{xx}\zeta, \quad E_{yy} y \frac{\partial \zeta}{\partial y} \approx -E_{yy}\zeta, \tag{2.13}$$

for $\zeta = h_*$ and $\zeta = s_*$, under the assumption that $\frac{\partial}{\partial x}(E_{xx}x\zeta)$ and $\frac{\partial}{\partial y}(E_{yy}y\zeta)$ are small, which is true under our assumption that the perturbations decay away from the origin.

To account for changes in ice geometry, we linearise the upper and lower surface boundary conditions at $z = \bar{h} + h_*$ and $z = \bar{s} + s_*$ onto $z = H$ and $z = 0$, respectively. The vanishing normal stress condition in (2.3) is approximated at $z = H$ by

$$p_* - 2\bar{\eta}\frac{\partial w_*}{\partial z} = h_* \rho_\mathrm{i}\, g, \tag{2.14}$$

where we have assumed that $|H - \bar{h}|$ is small. Similarly, the normal stress condition at the base (2.4) is approximated at $z = 0$ by

$$p_* - 2\bar{\eta}\frac{\partial w_*}{\partial z} = -s_* \Delta\rho\, g \tag{2.15}$$

where $\Delta\rho = \rho_\mathrm{w} - \rho_\mathrm{i}$ is the density difference between ice and water and we have assumed that $|\bar{s}|$ is small. The vanishing shear-stress conditions in (2.3) and (2.4) take the form

$$\frac{\partial u_*}{\partial z} + \frac{\partial w_*}{\partial x} = 2\frac{\partial \zeta}{\partial x}(2E_{xx} + E_{yy}) \tag{2.16}$$

$$\frac{\partial v_*}{\partial z} + \frac{\partial w_*}{\partial y} = 2\frac{\partial \zeta}{\partial y}(2E_{yy} + E_{xx}) \tag{2.17}$$

with $\zeta = h_*$ at the surface and $\zeta = s_*$ at the base. The terms on the right side of (2.16) and (2.17) arise from the projection of the stress tensor onto the perturbed surfaces [50,54]. We drop the asterisk subscripts on the perturbed fields below.

A primary goal in the analysis below is to determine when the perfect flotation condition

$$h = -\delta s \tag{2.18}$$

is satisfied locally, where we have defined the flotation factor

$$\delta \equiv \frac{\rho_\mathrm{w}}{\rho_\mathrm{i}} - 1. \tag{2.19}$$

The perfect flotation condition (2.18) corresponds to a purely hydrostatic state (Figure 1b). However, deviatoric (bridging) stresses within the ice can support departures from this state

royalsocietypublishing.org/journal/rspa Proc R Soc A 0000000

[37–39](Figure 1c). While our analysis is focused on ice-shelf topography, testing whether or not the horizontal velocity is depth-independent is also possible in this framework.

(c) Fourier transform approach

We apply Fourier transforms with respect to the horizontal coordinates (x, y) to simplify the system (2.9)-(2.17). The Stokes equations (2.9)-(2.10), written component-wise, transform to

$$-ik_x\widehat{p} + \bar{\eta}\left(-k^2\widehat{u} + \frac{\partial^2\widehat{u}}{\partial z^2}\right) = 0 \tag{2.20}$$

$$-ik_y\widehat{p} + \bar{\eta}\left(-k^2\widehat{v} + \frac{\partial^2\widehat{v}}{\partial z^2}\right) = 0 \tag{2.21}$$

$$-\frac{\partial\widehat{p}}{\partial z} + \bar{\eta}\left(-k^2\widehat{w} + \frac{\partial^2\widehat{w}}{\partial z^2}\right) = 0 \tag{2.22}$$

$$ik_x\widehat{u} + ik_y\widehat{v} + \frac{\partial\widehat{w}}{\partial z} = 0, \tag{2.23}$$

where $\boldsymbol{k} = [k_x, k_y]^{\mathrm{T}}$ is the horizontal wavevector with magnitude $k = \sqrt{k_x^2 + k_y^2}$. Equations (2.20)-(2.23) reduce to a fourth-order equation for the transformed vertical velocity [54],

$$\frac{\partial^4\widehat{w}}{\partial z^4} - 2k^2\frac{\partial^2\widehat{w}}{\partial z^2} + k^4\widehat{w} = 0. \tag{2.24}$$

The general solution to (2.24) is

$$\widehat{w} = \frac{c_1}{k}e^{kz} + \frac{c_2}{k}e^{-kz} + c_3ze^{kz} + c_4ze^{-kz}, \tag{2.25}$$

where the coefficients c_j depend on k. To determine the coefficients in (2.24), we rewrite all of the boundary conditions in terms of $\widehat{w}$. The shear-stress conditions (2.16) and (2.17) along with the transformed incompressibility condition (2.23) imply that

$$\frac{\partial^2\widehat{w}}{\partial z^2} + k^2\widehat{w} = \left[4k^2E - 2k_y^2E_{xx} - 2k_x^2E_{yy})\right]\widehat{\zeta} \tag{2.26}$$

at $\zeta = h$ and $\zeta = s$. The transformed normal-stress condition at the upper surface can be rewritten using (2.20)-(2.23) as

$$\bar{\eta}\left(3k^2\frac{\partial\widehat{w}}{\partial z} - \frac{\partial^3\widehat{w}}{\partial z^3}\right) = -k^2\rho_{\mathrm{i}}g\widehat{h}, \tag{2.27}$$

and, similarly, the transformed normal-stress condition at the base becomes

$$\bar{\eta}\left(3k^2\frac{\partial\widehat{w}}{\partial z} - \frac{\partial^3\widehat{w}}{\partial z^3}\right) = k^2\Delta\rho g\widehat{s}. \tag{2.28}$$

We insert the formula for $\widehat{w}$ (2.25) into the boundary conditions (2.26)-(2.28) to obtain a linear system for the coefficients c_j,

$$\begin{bmatrix} e^{k'} & -e^{-k'} & k'e^{k'} & -k'e^{-k'} \\ e^{k'} & e^{-k'} & (k'+1)e^{k'} & (k'-1)e^{-k'} \\ 1 & -1 & 0 & 0 \\ 1 & 1 & 1 & -1 \end{bmatrix}\begin{bmatrix} c_1 \\ c_2 \\ c_3 \\ c_4 \end{bmatrix} = \frac{\rho_{\mathrm{i}}g}{2\bar{\eta}}\begin{bmatrix} -\widehat{h} \\ (2\gamma - \gamma_0)k'\,\widehat{h} \\ \delta\widehat{s} \\ (2\gamma - \gamma_0)k'\,\widehat{s} \end{bmatrix}, \tag{2.29}$$

where the scaled wavevector magnitude,

$$k' = kH, \tag{2.30}$$

appears due to evaluation of the boundary conditions at $z = H$. In equation (2.29), we have defined the extensional parameters

$$\gamma = E t_\mathrm{r} \tag{2.31}$$

$$\gamma_0 = \frac{E_{yy} t_\mathrm{r} k_x'^2 + E_{xx} t_\mathrm{r} k_y'^2}{k'^2} \tag{2.32}$$

where

$$t_\mathrm{r} = \frac{2\bar{\eta}}{\rho_\mathrm{i} g H}, \tag{2.33}$$

is a characteristic timescale for the relaxation of surface topography due to viscous flow [55,56]. Thus, γ is a ratio of the timescale of topographic decay from viscous flow to the timescale set by extension. In the analysis below, we compare the timescale t_r to an intrinsic timescale that arises from competition between topographic relaxation and buoyancy, along with the extensional timescale set by the thinning rate E. Despite our idealised Newtonian treatment, the topographic decay time scale could be expected to vary across an ice shelf in practice because the effective viscosity of ice depends on temperature and strain rate [36]. The quantity γ_0 (2.32) vanishes in the case of uniform unidirectional extension (e.g., $E_{yy} = k_y = 0$) and approaches γ in the case of radial spreading ($E_{xx} = E_{yy}$).

We solve the linear system (2.29) for the coefficients c_j for all $k' > 0$. In the limit $k' \to 0$, the system is singular, meaning that the long-wavelength component of $\widehat{w}$ is not uniquely determined by the momentum balance alone. We show that solutions to the coupled problem are well-defined in the limit $k' \to 0$ because the surface evolution equations (2.11) and (2.12) impose additional constraints on the vertical velocity in relation to the surface elevations and melting rate. A necessary condition for the existence of solutions to (2.29) is that $\widehat{h} \to -\delta\widehat{s}$ as $k' \to 0$, or, equivalently,

$$\int_{-\infty}^{+\infty}\int_{-\infty}^{+\infty} h \,\mathrm{d}x\,\mathrm{d}y = -\int_{-\infty}^{+\infty}\int_{-\infty}^{+\infty} \delta s \,\mathrm{d}x\,\mathrm{d}y. \tag{2.34}$$

The condition (2.34) implies that that the perturbations will satisfy the perfect flotation condition, $h = -\delta s$, on average, but not necessarily locally.

Substituting the coefficients c_j into (2.25), we obtain an expression for the vertical velocity at the upper surface,

$$\widehat{w}|_{z=H} = -\frac{1}{t_\mathrm{r}}[\mathsf{R} + (2\gamma - \gamma_0)\mathsf{R}_0]\widehat{h} - \frac{1}{t_\mathrm{r}}[\delta\mathsf{B} + (2\gamma - \gamma_0)\mathsf{B}_0]\,\widehat{s}, \tag{2.35}$$

where the surface relaxation function R is given by

$$\mathsf{R} = \frac{e^{4k'} + 4k'e^{2k'} - 1}{k'[e^{4k'} - 2(1 + 2k'^2)e^{2k'} + 1]}, \tag{2.36}$$

and the buoyancy transfer function B is given by

$$\mathsf{B} = \frac{2(k'+1)e^{3k'} + 2(k'-1)e^{k'}}{k'[e^{4k'} - 2(1 + 2k'^2)e^{2k'} + 1]}. \tag{2.37}$$

The functions

$$\mathsf{R}_0 = \frac{4k'^3 e^{2k'}}{k'(e^{4k'} - 2(1 + 2k'^2)e^{2k'} + 1)} \tag{2.38}$$

and

$$\mathsf{B}_0 = \frac{2k'^2 e^{k'}(e^{2k'} - 1)}{k'(e^{4k'} - 2(1 + 2k'^2)e^{2k'} + 1)} \tag{2.39}$$

are contributions to the relaxation and transfer functions due to the extensional background state. We show that the extensional contributions R_0 and B_0 are negligible compared to R and B when the thinning rate is small, which allows for a simplified mathematical analysis.

Combining (2.11) and (2.35), the upper surface evolves according to

$$\frac{\partial \widehat{h}}{\partial t} + i(\boldsymbol{k}\cdot\bar{\boldsymbol{u}}_0)\widehat{h} = -\frac{1}{t_\mathrm{r}}[\mathsf{R} + (2\gamma-\gamma_0)\mathsf{R}_0]\widehat{h} - \frac{1}{t_\mathrm{r}}[\delta\mathsf{B} + (2\gamma-\gamma_0)\mathsf{B}_0]\,\widehat{s} + \frac{1}{t_\mathrm{r}}\gamma\widehat{h}. \tag{2.40}$$

where we have defined $\bar{\boldsymbol{u}}_0 = [\bar{u}_0, \bar{v}_0]^T$. Similarly, the vertical velocity at the lower surface is given by

$$\widehat{w}|_{z=0} = -[\delta\mathsf{R} + (2\gamma-\gamma_0)\mathsf{R}_0]\widehat{s} - [\mathsf{B} + (2\gamma-\gamma_0)\mathsf{B}_0]\widehat{h} \tag{2.41}$$

which, along with (2.12), leads to the evolution equation

$$\frac{\partial \widehat{s}}{\partial t} + i(\boldsymbol{k}\cdot\bar{\boldsymbol{u}}_0)\widehat{s} = \widehat{m} - \frac{1}{t_\mathrm{r}}[\delta\mathsf{R} + (2\gamma-\gamma_0)\mathsf{R}_0]\widehat{s} - \frac{1}{t_\mathrm{r}}[\mathsf{B} + (2\gamma-\gamma_0)\mathsf{B}_0]\,\widehat{h} + \frac{1}{t_\mathrm{r}}\gamma\widehat{s} \tag{2.42}$$

Equations (2.40) and (2.42) show that the upper and basal surfaces evolve according to a competition between topographic decay that is captured by the R functions, buoyancy forcing that is captured by the B functions, and extensional thinning from the $\gamma\widehat{h}$ and $\gamma\widehat{s}$ terms. The buoyancy function B transmits perturbations between the upper and basal surfaces, similar to transfer functions in previous models of grounded ice [53,54].

The relaxation function (2.36) and buoyancy function (2.37) are singular in the limit $k \to 0$ (Figure 2). Physically, these singularities imply that topographic relaxation and buoyancy adjustments occur instantaneously at long wavelengths under the assumption of an infinitely expansive ice shelf. Laurent expansions of R and B indicate that they grow like k^{-4} as $k \to 0$ in accordance with the similar crevasse evolution model [47]. We show that the solutions are well-defined despite the singularities. For the purpose of computing the solutions below, we regularise the functions R and B so that the long-wavelength limit of the dominant eigenvalue in the problem is attained at a small value of k (Appendix A). Below, we will show that the asymptotic behaviour $\mathsf{R} \sim \mathsf{B}$ at long wavelengths is associated with a hydrostatic state because topographic relaxation is perfectly balanced by buoyancy.

At short wavelengths, the behaviour $\mathsf{R} \gg \mathsf{B}$ can lead to diminished surface topography because the presence of deviatoric stresses causes the topographic relaxation to exceed the buoyancy forcing (Figure 2). In particular, the behaviour $\mathsf{R} \sim k^{-1}$ at short wavelengths agrees with classical models of postglacial rebound where the mantle is modelled as a viscous layer with infinite thickness [55]. The extensional contributions R_0 and B_0 behave like k^{-2} as $k \to 0$ and e^{-k} as $k \to \infty$ (Figure 2b). Thus, these terms can be neglected for small values of γ. The extensional terms enhance the effects of buoyancy relative to relaxation because $\mathsf{B}_0 > \mathsf{R}_0$, which can influence the non-hydrostatic effects and stability at larger values of γ.

(d) Scaling and simplification

Now, we introduce a scaling for the model equations (2.40) and (2.42). We scale the variables according to

$$h = Hh', \quad s = Hs', \quad x = Hx', \quad \boldsymbol{k} = H^{-1}\boldsymbol{k}', \quad t = t_\mathrm{r}t', \quad m = {t_\mathrm{r}}^{-1}Hm', \tag{2.43}$$

where the viscous relaxation time scale t_r is defined in (2.33). Omitting primes, equations (2.40) and (2.42) become

$$\frac{\partial \widehat{h}}{\partial t} + i(\boldsymbol{k}\cdot\boldsymbol{\alpha})\widehat{h} = -[\mathsf{R} + (2\gamma-\gamma_0)\mathsf{R}_0]\widehat{h} - [\delta\mathsf{B} + (2\gamma-\gamma_0)\mathsf{B}_0]\,\widehat{s} + \gamma\widehat{h}. \tag{2.44}$$

$$\frac{\partial \widehat{s}}{\partial t} + i(\boldsymbol{k}\cdot\boldsymbol{\alpha})\widehat{s} = \widehat{m} - [\delta\mathsf{R} + (2\gamma-\gamma_0)\mathsf{R}_0]\widehat{s} - [\mathsf{B} + (2\gamma-\gamma_0)\mathsf{B}_0]\,\widehat{h} + \gamma\widehat{s}, \tag{2.45}$$

where the parameter

$$\boldsymbol{\alpha} = \frac{\bar{\boldsymbol{u}}_0 t_\mathrm{r}}{H} \tag{2.46}$$

is the advective component of the background flow velocity relative to the velocity scale H/t_r. Below, we show that solutions evolve over a longer time scale $t_\mathrm{e} \equiv t_\mathrm{r} \times 2\left(1+\delta^{-1}\right)$, which coincides with the characteristic time scale in shallow approximations of ice-shelf flow [57].

We derive a simplified system under the assumption that the extensional contributions to the relaxation and buoyancy functions satisfy $(2\gamma-\gamma_0)\mathsf{R}_0 \ll \mathsf{R}$ and $(2\gamma-\gamma_0)\mathsf{B}_0 \ll \mathsf{B}$ and can, therefore, be neglected. This approximation is accurate for small values of the extensional parameter γ (Figure 2b). Here, we focus on the effects of across-channel advection and set $\bar{v}_0 = 0$ because the melt rate does not vary in the along-channel direction for the examples explored herein (Figure 1). Along-channel advection ($\bar{v}_0 > 0$) does not have an effect when there are no along-channel variations because the problem can be translated to a frame moving with $\bar{v}_0$ where the melt rate remains the same. By including an across-channel advective component $\bar{u}_0 \geq 0$, we are assuming that the melt rate does not necessarily advect with the basal topography perturbation. For example, a stationary melt source that the ice advects over could arise from a subglacial outflow plume [7]. We revisit this issue in the discussion.

Under these assumptions, equations (2.44) and (2.45) simplify to

$$\frac{\partial \widehat{h}}{\partial t} + ik_x\alpha\widehat{h} = -\mathsf{R}\widehat{h} - \mathsf{B}\delta\widehat{s} + \gamma\widehat{h} \tag{2.47}$$

$$\frac{\partial \widehat{s}}{\partial t} + ik_x\alpha\widehat{s} = \widehat{m} - \mathsf{R}\delta\widehat{s} - \mathsf{B}\widehat{h} + \gamma\widehat{s} \tag{2.48}$$

where $\alpha = \bar{u}_0 t_\mathrm{r}/H$. We have retained the growth terms, γh and γs, to explore the effect of extension on the stability of topography. While we have made these approximations to simplify the presentation, solutions to the full problem (2.44)-(2.45) can be obtained by following the same spectral decomposition argument that we employ below. As we have neglected terms that only arise during extension, the system (2.47)-(2.48) can be viewed as a quasi-cryostatic, Newtonian simplification of the previous linearised extension model [47], although we have extended this to include an advective component in the across-channel direction. The simplified mathematical structure of (2.47)-(2.48) allows us to analyse the solutions in detail and derive a Green's function for a certain class of steady-state solutions.

3. Analysis

Next, we derive solutions to the problem (2.47)-(2.48) via a spectral decomposition. We analyse the stability of steady-state channels, time scales of channel evolution, and the role of the extensional parameter γ. We also quantify when solutions can be expected to deviate from the perfect flotation condition, $h = -\delta s$. We then derive steady solution formulas and find a Green's function for a one-dimensional melt channel in the absence of background advection and extension. While our focus is on topography, velocity solutions can be derived and analysed once the elevations h and s are obtained. We provide expressions for the vertical and horizontal velocity solutions in Appendix B and C, respectively.

(a) Solution formulas

We rewrite the system (2.47)-(2.48) as

$$\frac{\partial \boldsymbol{y}}{\partial t} = \mathbf{A}\boldsymbol{y} + \boldsymbol{b}, \tag{3.1}$$

where

$$\boldsymbol{y} = \begin{bmatrix} \widehat{h} \\ \widehat{s} \end{bmatrix}, \quad \boldsymbol{b} = \begin{bmatrix} 0 \\ \widehat{m} \end{bmatrix}, \quad \mathbf{A} = -\begin{bmatrix} ik_x\alpha - \gamma + \mathsf{R} & \delta\mathsf{B} \\ \mathsf{B} & ik_x\alpha - \gamma + \delta\mathsf{R} \end{bmatrix}. \tag{3.2}$$

royalsocietypublishing.org/journal/rspa Proc R Soc A 0000000

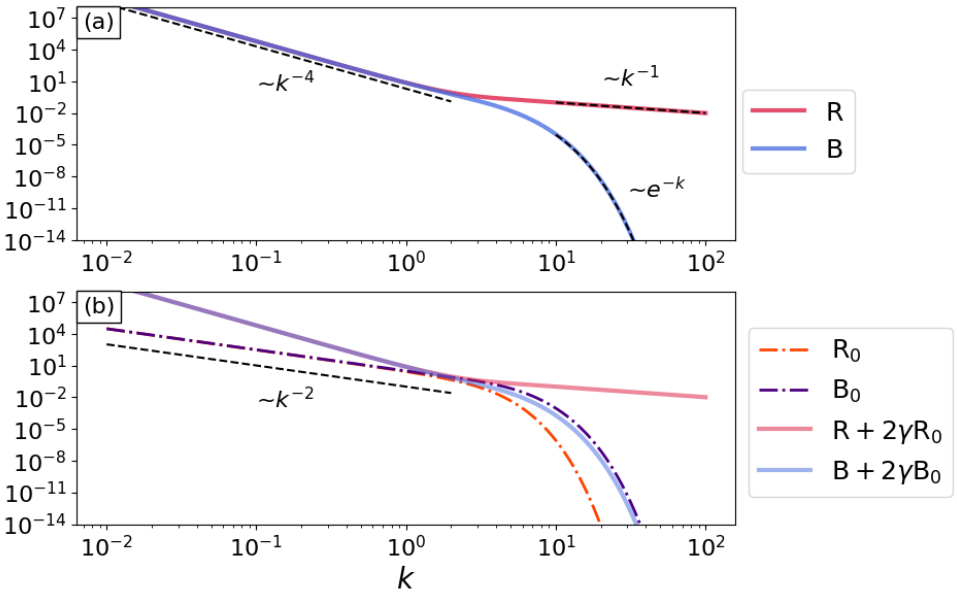

Figure 2. (a) Graphs of R (2.36) and B (2.37) as functions of k (nondimensional) along with their asymptotic behaviours as $k \to 0$ and $k \to \infty$ (dashed lines). (b) Extensional contributions R_0 and B_0 to the full relaxation and buoyancy functions $R + (2\gamma - \gamma_0)R_0$ and $B + (2\gamma - \gamma_0)B_0$, which are plotted for $\gamma = 0.05$ and $\gamma_0 \equiv 0$. The extensional contributions are negligible for this value of γ.

To derive solutions and analyse their basic properties, we diagonalise the matrix **A** according to

$$\mathbf{A} = \mathbf{P}\mathbf{D}\mathbf{P}^{-1}, \quad \mathbf{P} = \begin{bmatrix} | & | \\ \boldsymbol{\varphi}_- & \boldsymbol{\varphi}_+ \\ | & | \end{bmatrix}, \quad \mathbf{D} = \begin{bmatrix} \lambda_- & 0 \\ 0 & \lambda_+ \end{bmatrix}. \tag{3.3}$$

The eigenvalues ($\lambda_\pm$) and eigenvectors ($\boldsymbol{\varphi}_\pm$) of **A** in (3.3) are

$$\lambda_\pm = \gamma - \left(ik_x\alpha - \frac{\delta+1}{2}\mathsf{R} \mp \frac{\mu}{2} \right) \tag{3.4}$$

$$\boldsymbol{\varphi}_\pm = \begin{bmatrix} \frac{\mathsf{R}(1-\delta)\mp\mu}{2\mathsf{B}} \\ 1 \end{bmatrix} \tag{3.5}$$

where we have defined

$$\mu = \sqrt{4\delta\mathsf{B}^2 + \mathsf{R}^2(\delta-1)^2}. \tag{3.6}$$

The eigenvector corresponding to the dominant eigenvalue λ_+ has the limit $\boldsymbol{\varphi}_+/\|\boldsymbol{\varphi}_+\| \to [-\delta, 1]^T$ as $k \to 0$, which drives the solution towards the perfect flotation condition $h = -\delta s$ (Figure 3 and Figure 4). The other eigenpair encourages deviations from perfect flotation, but this effect decays rapidly as $k \to 0$ since λ_- becomes very negative (Figure 3). However, we show below that these effects can be important at short wavelengths. The normalised eigenvectors approach $\boldsymbol{\varphi}_+/\|\boldsymbol{\varphi}_+\| \to [0, 1]^T$ and $\boldsymbol{\varphi}_-/\|\boldsymbol{\varphi}_-\| \to [1, 0]^T$ as $k \to \infty$, meaning that the surface and basal responses become decoupled at short wavelengths because perturbations are not transmitted through the ice column.

In the absence of thinning, steady-state solutions are stable because the eigenvalues of **A** have negative real part when $\gamma = 0$. Equation (3.4) implies that $\mathrm{Re}(\lambda_-) < 0$ and $\mathrm{Re}(\lambda_+) < 0$ if and only if $\mathsf{R} > \mathsf{B}$, which is satisfied for all $k > 0$ (Figure 2). The long-wavelength limit of the dominant

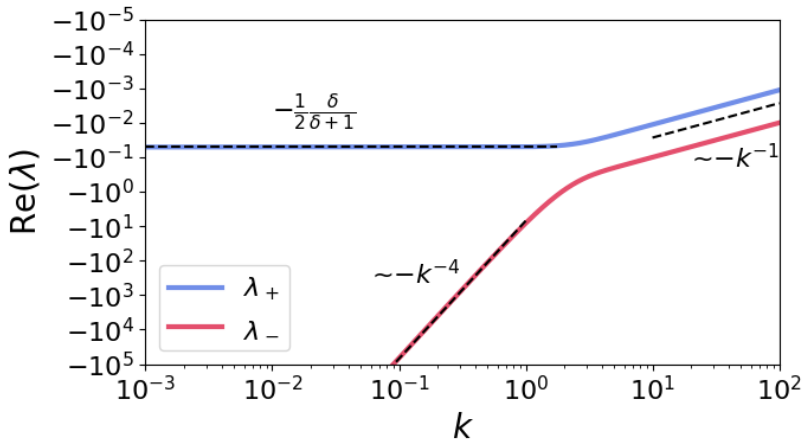

Figure 3. Real parts of the eigenvalues ($\lambda_\pm$) of **A** from equation (3.4) along with their asymptotic behaviours as $k \to 0$ and $k \to \infty$ (dashed lines) in the absence of extension ($\gamma = 0$). Imaginary components of the eigenvalues are only present when across-channel advection is nonzero ($\alpha > 0$). The real parts of the eigenvalues are shifted towards positive values when the extensional parameter is positive ($\gamma > 0$).

eigenvalue is

$$\lim_{k\to 0} \lambda_+\Big|_{\gamma=0} = -\frac{1}{2}\left(\frac{\delta}{\delta+1}\right), \tag{3.7}$$

when $\gamma = 0$, although this limit is approximately attained for $k \lesssim 1$ (Figure 3). This limit shows that solutions will tend to evolve over the longer timescale t_e defined by

$$t_\mathrm{e} \equiv t_\mathrm{r} \times 2\left(1 + \frac{1}{\delta}\right) = \frac{4\eta}{\Delta\rho\, g H}\frac{\rho_\mathrm{w}}{\rho_\mathrm{i}}, \tag{3.8}$$

which is a characteristic timescale in shallow approximations of ice-shelf flow [57]. The timescale t_e (3.8) properly accounts for the competition between topographic relaxation and buoyancy in contrast to the original timescale t_r (2.33) that does not include the density difference between ice and water. In particular, the intrinsic time scale t_e exceeds t_r because the topographic relaxation at the upper surface must coincide with topographic relaxation at the lower surface due to buoyancy, meaning that more mass must be redistributed relative to the case where there is a single free surface as in, for example, the classical postglacial rebound problem [55]. While longer-wavelength solutions reach steady state according to the time scale t_e, shorter-wavelength solutions will take longer to reach steady state because the eigenvalues become diminished as $k \to \infty$ (Figure 3).

When the extensional parameter is positive ($\gamma > 0$), equation (3.4) shows that the real parts of the eigenvalues are shifted towards positive values so that instability will arise first at shorter wavelengths (Figure 3). All wavelengths are unstable when $\gamma > \frac{1}{2}\delta/(\delta+1)$. In physical terms, this occurs when the intrinsic channel evolution timescale exceeds the time scale from the background strain rate, $t_\mathrm{e} > 1/E$. This long-wavelength stability ratio $1/(t_\mathrm{e}E)$ is the same as the stability parameter S_0 from [47] when the effects of snow density at the upper surface are neglected. When $\gamma < \frac{1}{2}\delta/(\delta+1)$, the stability of the solution depends sensitively on the spectral properties of the melt rate m. In particular, stable steady solutions are possible for $\gamma < \frac{1}{2}\delta/(\delta+1)$ if $\widehat{m}$ is rapidly decaying to zero at the wavelength where the instability arises.

Assuming no initial perturbation, the solution to (3.1) is

$$\boldsymbol{y} = \int_0^t e^{\mathbf{A}(t-\tilde{t})}\boldsymbol{b}(\tilde{t})\,\mathrm{d}\tilde{t}, \tag{3.9}$$

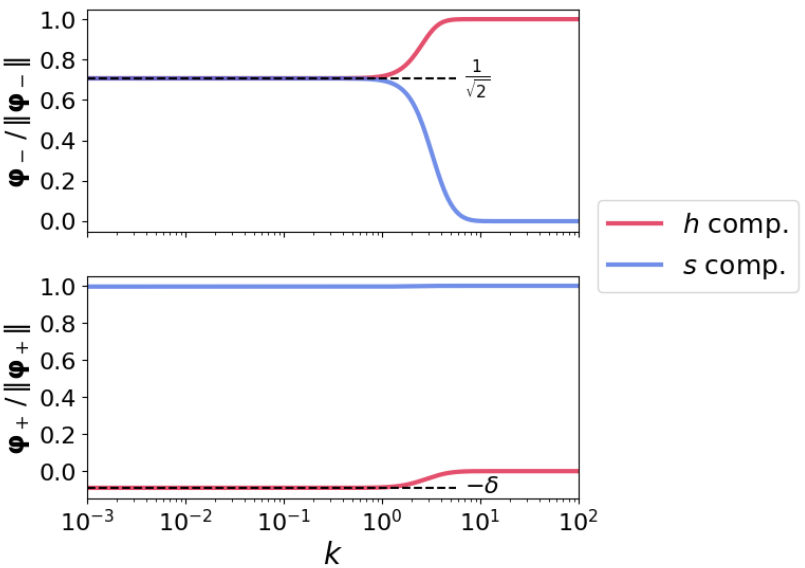

Figure 4. Normalised eigenvectors ($\boldsymbol{\varphi}_\pm$) of $\mathbf{A}$. 'h comp.' is the first vector component and 's comp.' is the second component in accordance with (3.2). Dashes lines highlight analytical limits.

where we compute the matrix exponential via $e^{\mathbf{A}t} = \mathbf{P}e^{\mathbf{D}t}\mathbf{P}^{-1}$. Equation (3.9) shows that the solution for the ice-surface elevation anomaly is

$$\widehat{h} = \int_0^t \mathsf{K}_h(t-\tilde{t})\widehat{m}(\tilde{t})\,\mathrm{d}\tilde{t},$$
$$\mathsf{K}_h(t) \equiv -\frac{\delta \mathsf{B}}{\mu}(e^{\lambda_+ t} - e^{\lambda_- t}). \tag{3.10}$$

Similarly, the solution for the elevation anomaly at the ice-water interface is

$$\widehat{s} = \int_0^t \mathsf{K}_s(t-\tilde{t})\widehat{m}(\tilde{t})\,\mathrm{d}\tilde{t},$$
$$\mathsf{K}_s(t) \equiv \frac{1}{2\mu}[(\mu + (1-\delta)\mathsf{R})e^{\lambda_+ t} + (\mu - (1-\delta)\mathsf{R})e^{\lambda_- t}]. \tag{3.11}$$

The formulas (3.10) and (3.11) show that $\widehat{h}$ will be close to $-\delta\widehat{s}$ provided that K_h is close to $-\delta\mathsf{K}_s$ and $|\widehat{m}|$ is not too large. We show the kernels K_s and $-\mathsf{K}_h/\delta$ in Figure 5, highlighting that $\mathsf{K}_h(k,t) \approx -\delta\mathsf{K}_s(k,t)$ when $k \in (0,1)$ and $t \in (10^{-1}, \infty)$. Therefore, significant deviations from perfect flotation only occur on fast timescales relative to the relaxation timescale or short wavelengths relative to the ice thickness.

Finally, across-channel advection from the background flow, which is described by the α parameter, can produce asymmetry and smaller surface perturbations. In the fast-flow limit ($\alpha \to \infty$), the perturbations decay to zero because the integral kernels in (3.10) and (3.11) become highly oscillatory due to the imaginary parts of the eigenvalues in (3.4). This limit occurs when the ice advects with the background flow too quickly to be disrupted by basal melting or freezing perturbations. After deriving steady solutions, we illustrate through several examples how the evolution and stability of topography is affected by across-channel advection, extension, and the spectral properties of the melt rate.

royalsocietypublishing.org/journal/rspa Proc R Soc A 0000000

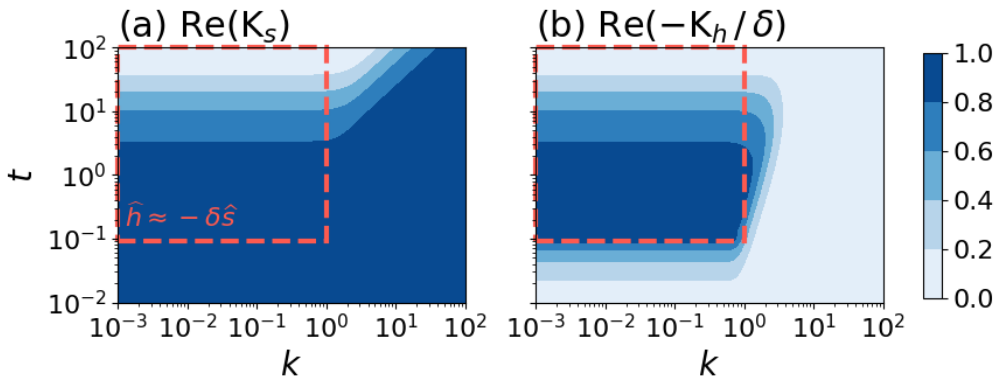

Figure 5. Real parts of the kernels K_s (3.11) and $-\mathsf{K}_h/\delta$ (3.10) of the solution operators in the absence of extension ($\gamma = 0$). The dashed boxes denote the region in (k, t) space where the flotation thickness is approximately satisfied since $\mathsf{K}_h \approx -\delta\mathsf{K}_s$. Imaginary parts of the kernels only arise when across-channel advection is present ($\alpha > 0$).

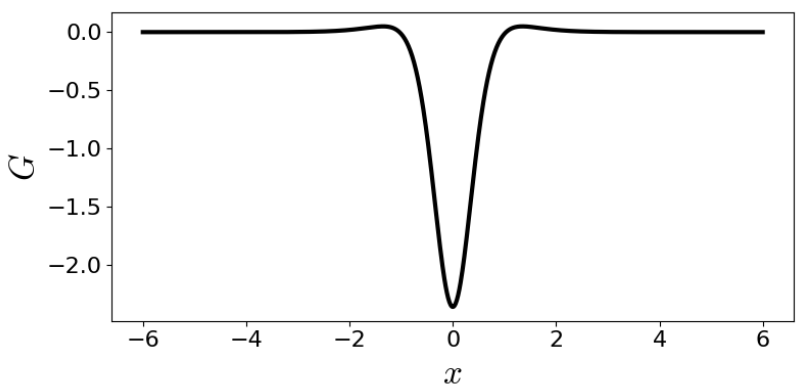

Figure 6. Graph of the free-space Green's function G given by equation (3.17).

(b) Steady states

We compute steady solutions via $[\widehat{h}_\mathrm{e}, \widehat{s}_\mathrm{e}]^\mathrm{T} = -\mathbf{A}^{-1}\boldsymbol{b}$ to obtain

$$\widehat{h}_\mathrm{e} = -\frac{\delta \mathsf{B}\widehat{m}}{\delta(\mathsf{R}^2 - \mathsf{B}^2) + (ik_x\alpha - \gamma)(\delta+1)\mathsf{R} + (ik_x\alpha - \gamma)^2} \tag{3.12}$$

$$\widehat{s}_\mathrm{e} = \frac{(\mathsf{R} + ik_x\alpha - \gamma)\widehat{m}}{\delta(\mathsf{R}^2 - \mathsf{B}^2) + (ik_x\alpha - \gamma)(\delta+1)\mathsf{R} + (ik_x\alpha - \gamma)^2}. \tag{3.13}$$

We derive a free-space Green's function for the steady problem in the limits of no background advection ($\alpha = 0$), no thinning ($\gamma = 0$), and no variations in the y direction (i.e., $k = |k_x|$). Under these assumptions, we obtain

$$\widehat{h}_\mathrm{e} = \widehat{G}\,\widehat{m}. \tag{3.14}$$

where

$$\widehat{G} \equiv -\frac{\mathsf{B}}{\mathsf{R}^2 - \mathsf{B}^2} = -k^2\coth(k)\mathrm{csch}(k) - k\,\mathrm{csch}(k). \tag{3.15}$$

royalsocietypublishing.org/journal/rspa Proc R Soc A 0000000

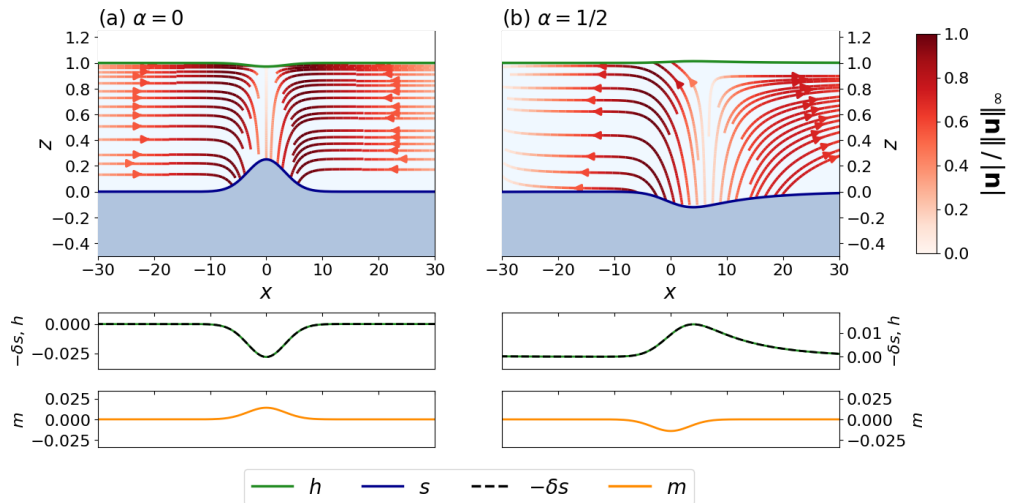

Figure 7. Steady ice-shelf profiles highlighting the flow field and topography in the limit of no background extension ($\gamma = 0$). Normalised velocity streamlines are plotted on the deformed grid defined by $z \mapsto (1-z)s + zh$. The elevation (green) and perfect flotation elevation $-\delta s$ (dashed black) are shown for each example, along with the melting or freezing rate m (orange). For both examples, the standard deviation of the melting rate is $\sigma = 10/3$.

We use the convolution theorem to find the steady surface elevation via

$$h_e(x) = \int_{-\infty}^{+\infty} G(x-\tilde{x}) m(\tilde{x})\, \mathrm{d}\tilde{x}, \tag{3.16}$$

where the free-space Green's function is

$$G(x) = \frac{\pi}{4}\mathrm{sech}^2\left(\frac{\pi x}{2}\right)\left[\pi x \tanh\left(\frac{\pi x}{2}\right) - 3\right]. \tag{3.17}$$

In two horizontal dimensions, G corresponds to the steady elevation anomaly that arises when the melt rate is a line source (Figure 6).

4. Examples

We explore solutions to the model for different melt rates m, across-channel advection parameters α, and extensional parameters γ. In all of these examples, we choose a stationary Gaussian-shaped melting or freezing anomaly that does not vary with time or the y direction for simplicity and to facilitate comparison with previous modeling studies [38,39,47]. Therefore, we set $m = \pm m_0 \exp\left(-\frac{1}{2}x^2/\sigma^2\right)$ and choose an amplitude of $m_0 = 0.014$, which corresponds to a melt rate of 5 m/yr when $H = 500$ m, $\bar{\eta} = 10^{14}$ Pa s, and $\rho_i = 917$ kg/m^3. In all examples, we set $\delta = 0.11$, which corresponds to a sea water density of $\rho_w = 1020$ kg/m^3. With these parameters, the intrinsic channel evolution timescale given by t_e in equation (3.8) is $\sim$27 yr and the critical value of the extension parameter above which instability is guaranteed is $\gamma = \frac{1}{2}\delta/(1+\delta) \approx 0.05$.

We first explore the effect of varying the across-channel advection parameter α, the width of the anomaly via σ, and the sign of the anomaly in the limit of no background extension, $\gamma = 0$ (Figure 7 and Figure 8). We set either $\alpha = 0$ or $\alpha = 1/2$, corresponding to no across-channel flow or an across-channel flow of $\bar{u} \approx 193$ m/yr with the parameters cited above, respectively. We also show streamlines of the steady flow fields for each example. Expressions for the vertical and horizontal velocity fields are provided in Appendix B and Appendix C, respectively.

When the melting anomaly is wide relative to the ice thickness ($\sigma = 10/3$), we find that the steady surface elevation closely matches the perfect flotation condition (Figure 7a). Introducing

royalsocietypublishing.org/journal/rspa Proc R Soc A 0000000

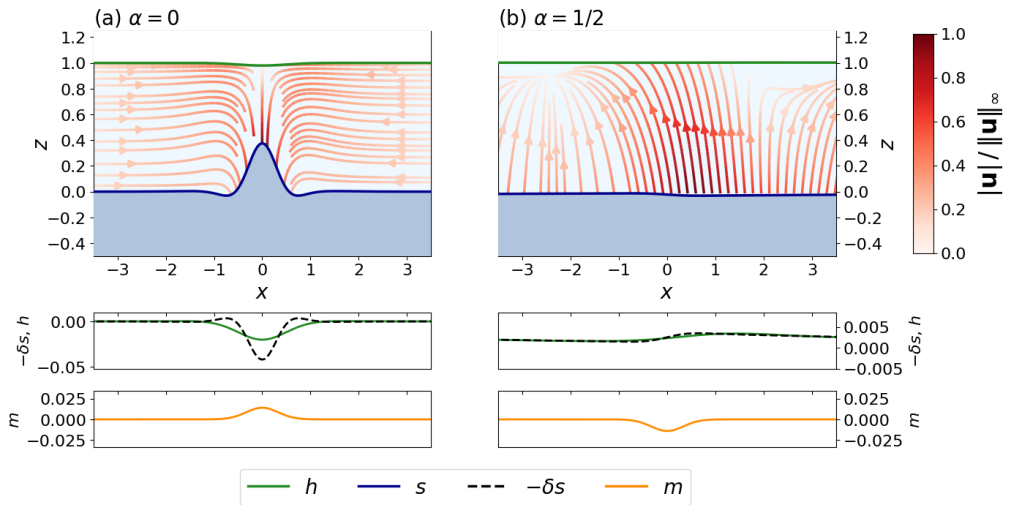

Figure 8. Same as Figure 7 except that the standard deviation of the melting rate is set to $\sigma = 1/3$. The ice-surface elevations (green lines) deviate from the perfect flotation condition (dashed lines).

background advection leads to asymmetry in the surfaces and flow fields (Figure 7b). Ice flows inwards to balance the melting anomaly (Figure 7a) and outwards to balance the freezing anomaly (Figure 7b). We find that significant deviations from perfect flotation ($h \neq -\delta s$) occur when the melting anomaly width approaches the ice thickness ($\sigma \approx 1/3$) or smaller. In this regime, the elevation anomaly is diminished relative to the perfect flotation elevation (Figure 8a). At these smaller length scales, across-channel advection from the background flow produces pronounced asymmetry and the surface expression of the basal anomaly is greatly diminished (Figure 8b).

We illustrate the stability and hydrostatic imbalance results further by first considering the transient evolution of the ice thickness for the narrow channel example ($\sigma = 1/3$) for a range of values of the extension parameter γ, up to the critical value of $\gamma = \frac{1}{2}\delta/(1+\delta) \approx 0.05$ where instability is guaranteed (Figure 9). For smaller values of the extension parameter, $\gamma \lesssim 0.01$, the channel approaches steady state after $t \approx 10\, t_e$ in dimensional terms (Figure 9a). Larger values of the extension parameter result in channels that are more deeply incised. When $\gamma \gtrsim 0.01$, the channels break through the ice column because viscous flow towards the channel is not able to overcome the extensional forcing. For larger γ, the channel incision can exceed the linearly extrapolated melt rate due to the effects of extension (Figure 9a). We also compare the ice thickness change to an ice thickness estimate based on the assumption of perfect flotation (Figure 9b). We find that an ice thickness estimate that is based on the perfect flotation assumption would underestimate the true ice thickness by as much as ∼20% of the background ice thickness when $\gamma = 0$ or up to ∼35% when $\gamma = 0.01$ (Figure 9c).

To explore these effects further, we repeated the above experiment for the wide channel example ($\sigma = 10/3$) and found that stable steady states exist for a wider range of extension parameters, $\gamma \lesssim 0.03$, relative to the narrow anomaly example (Figure 10). This difference arises because the stability depends on the spectral properties of the melt rate when $\gamma < \frac{1}{2}\delta/(1+\delta) \approx 0.05$. The wide melting anomalies are inherently more stable than the narrow anomalies because they are transformed to longer wavelengths in Fourier space that can avoid short-wavelength instabilities (Figure 3). For example, instability arises at $k \approx 3.7$ when $\gamma = 0.03$, which falls outside the "width" of $\widehat{m} \propto \exp(-k^2\sigma^2/2)$ when $\sigma = 10/3$ but not when $\sigma = 1/3$ (Figure 9a and Figure 10a). In physical terms, the wider channels generate a stronger secondary flow that can overcome the extensional forcing. Stability at stronger extensional regimes also allows wide channels to become more deeply incised at steady state relative to narrow channels (Figure 10b). The wide

royalsocietypublishing.org/journal/rspa Proc R Soc A 0000000

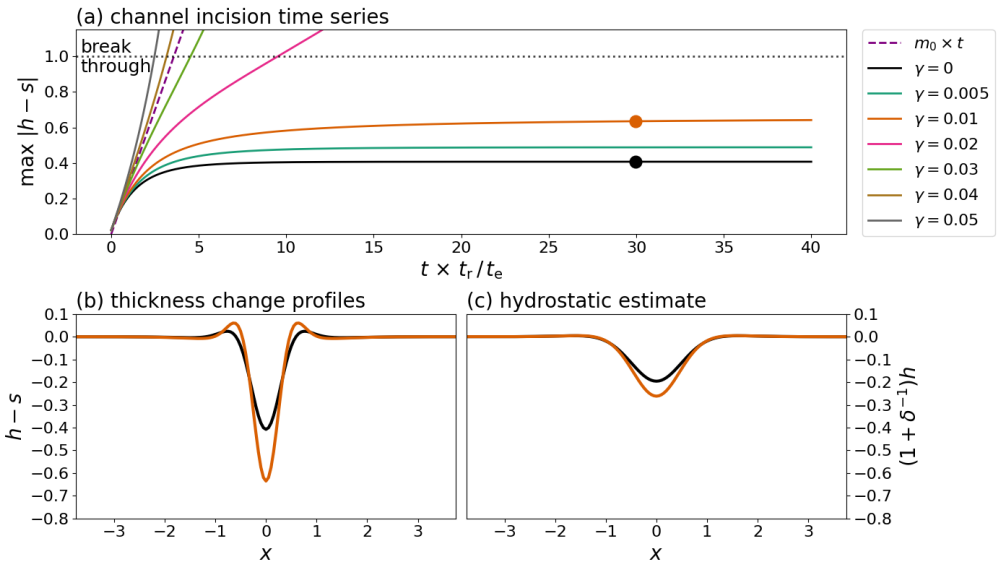

Figure 9. (a) Time series of the maximum channel incision for various values of the extensional parameter γ along with the linearly extrapolated maximum melt rate (dashed line). Time has been (re-)scaled relative to the intrinsic channel evolution time scale t_e. The parameters $\sigma = 1/3$ and $\alpha = 0$ are the same as in Figure 8a. Stability is found for small values of the extensional parameter, i.e., $\gamma \lesssim 0.01$. The melting rate and other parameters are the same as in Figure 8a. (b) Profiles of the thickness change at the time points indicated in (a) for $\gamma = 0$ (black) and $\gamma = 0.01$ (orange). (c) Thickness change estimated by assuming the surface elevation is in perfect flotation. When $\gamma = 0$, the steady thickness is underestimated by up to ~ 0.2, or $\sim$20% of the background ice thickness (H) in dimensional terms, relative to the true thickness change in (b). When $\gamma = 0.01$, the steady thickness is underestimated by up to $\sim$35%.

anomalies approach steady state by $t \approx 5\, t_e$, which more closely follows the intrinsic long-wavelength timescale than the narrow channel examples. We find that an ice thickness estimate based on the perfect flotation assumption would underestimate the true ice thickness by up to $\sim$3% of the background ice thickness for the stable values of $\gamma \lesssim 0.03$ shown here (Figure 9b).

Finally, we also compare the one-dimensional convolution solution (3.16) to a solution obtained by solving the fully nonlinear problem (2.1)-(2.6) with a finite element method [58]. In the nonlinear simulations, we relate the ice viscosity to strain rate through a regularised Glen's flow law [34–36]

$$\eta = \frac{1}{2} B (|\dot{\boldsymbol{\varepsilon}}|^2 + \nu)^{\frac{1-n}{2n}}, \tag{4.1}$$

where n is the stress exponent, B is the ice hardness parameter, $|\dot{\boldsymbol{\varepsilon}}| = \sqrt{\frac{1}{2}\dot{\boldsymbol{\varepsilon}} : \dot{\boldsymbol{\varepsilon}}}$ is the second invariant, and ν is a regularisation parameter that ensures finite viscosity in the limit of zero strain rate. In the flow law (4.1), we set the stress exponent to $n = 4$ and the ice hardness to $B = 10^8$ Pa s$^{1/n}$ following recent calibration of these parameters for Antarctic ice shelves [59]. We set the viscosity regularization parameter ν to coincide with the background viscosity $\bar{\eta} = 10^{14}$ Pa s at zero strain rate with these parameters. Thus, the viscosity in the nonlinear model only deviates from the linear model due to strain rates from the flow perturbations. On the side-walls of the computational domain, we set the horizontal velocity and vertical shear stress to zero. The computational domain is defined by a height of $H = 500$ m and width of 40 km, which is discretised by a uniform mesh with an element width of 100 m. The sea level is set to $\ell = (\rho_i/\rho_w)H$ in the lower-surface boundary condition (2.4). The velocity and pressure are approximated by Taylor-Hood elements [58]. To allow for steady-state solutions in this confined setting, we set a constant accumulation rate a in (2.5) that is equal to the average melt rate [39]. We have

royalsocietypublishing.org/journal/rspa Proc R Soc A 0000000

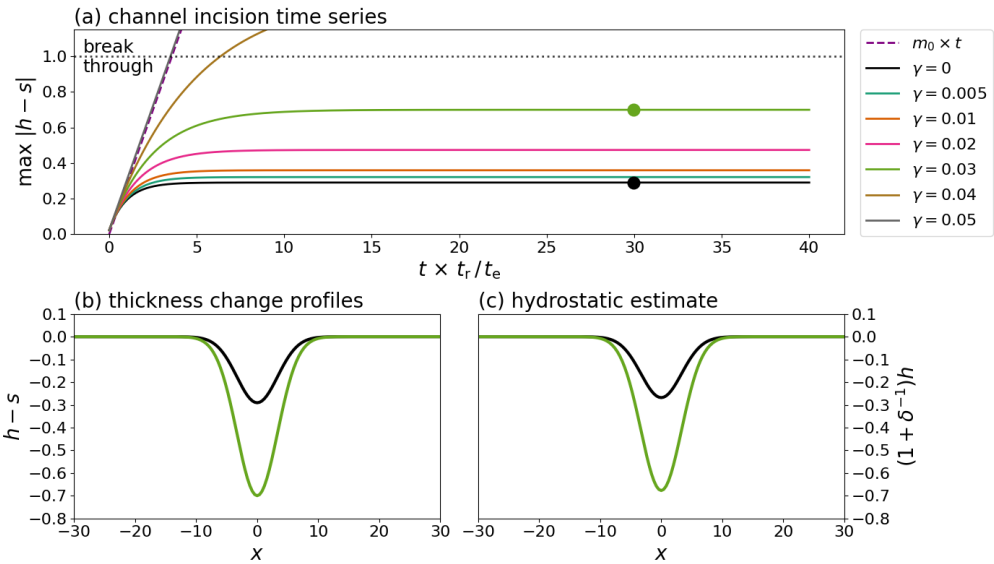

Figure 10. Same as Figure 9 except with the parameters $\sigma = 10/3$ and $\alpha = 0$ from Figure 7a. Stability is possible for larger values of the extensional parameter, i.e., $\gamma \lesssim 0.03$, relative to Figure 9. (b) Steady profiles are shown for $\gamma = 0$ (black) and $\gamma = 0.03$ (green). In (c), the hydrostatic thickness estimate is ~ 0.03 smaller than the true thickness change in (b), or 3% of the background ice thickness (H) in dimensional terms, for both values of γ.

implemented the finite element method in FEniCSx and made it openly available as described in the Data Availability statement [60–62].

We find that the nonlinear solution approaches steady state by $t = 5\,t_e$. For the parameters listed above, the finite element solution closely matches the Green's function solution (3.16) when the melt rate is small, e.g., 1 m/yr (Figure 11a). This agreement suggests that the Green's function solution could be used for verification of nonlinear Stokes models when the melt rate is small. When the melt rate is larger, there can be deviations between the Green's function solution and finite element solution due to nonlinearities in the original problem (2.1)-(2.6) and the lateral confinement in the numerical solution (Figure 11b). Deviations from a Newtonian viscous state in the nonlinear model is controlled by the rheology parameters B and n in the flow law (4.1), which also influence the agreement with the linearised model. Linearisation of the boundary conditions onto the simplified domain also contributes to the accuracy of the small-perturbation solutions when the channel incises through a significant fraction of the ice thickness (Figure 11b).

5. Discussion

The linearised analysis shows that short wavelength topography can deviate locally from perfect flotation even in steady state. These non-hydrostatic effects are due to the presence of non-negligible deviatoric (bridging) stresses. As the ice thickness is typically assumed to be in hydrostatic balance, non-hydrostatic effects can influence the accuracy of ice thickness and basal melt-rate estimates [38–40]. For example, recent numerical modelling showed that the true melt rate and hydrostatic melt-rate estimate can have a pointwise mismatch of up to 25%, although the total effect was less than 1% when integrated over the entire domain [39]. In these simulations, the accuracy of the integrated melt rate estimate could arise because the ice shelf satisfies the flotation condition in an averaged sense analogous to equation (2.34). Comparisons of hydrostatic thickness estimates with thickness from ice-penetrating radar showed a significant discrepancy across a channel on the Getz Ice Shelf in West Antarctica [40]. Similarly, we found that the

royalsocietypublishing.org/journal/rspa Proc R Soc A 0000000

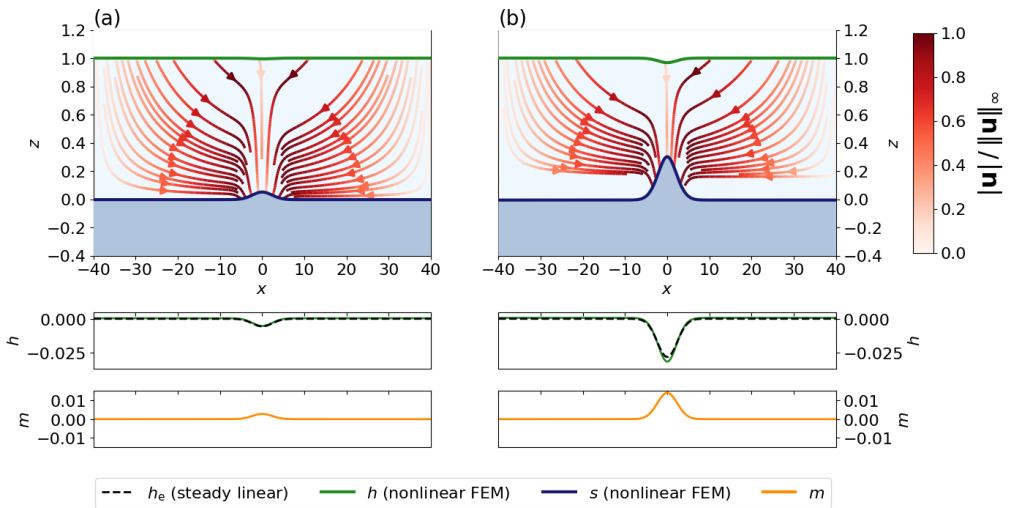

Figure 11. Nonlinear solutions obtained with a finite element method in one horizontal dimension for two different basal melting rates and no background extension. The melting rate in panel (b) is five times larger than the melting rate in panel (a). The finite element solutions are shown at time $t = 5\,t_e$ and have approached steady state. Steady state Green's function solutions h_e given by (3.16)-(3.17) are shown as dashed lines.

thickness can be underestimated significantly at short wavelengths under the perfect flotation assumption (Figure 9).

Incorporating hydrostatic imbalance into estimates of ice thickness and discharge could help to sharpen melt-rate estimates. The linearised model developed herein could potentially be used to invert for the basal melt rate from altimetry data while allowing for hydrostatic imbalance. For example, equation (3.10) suggests that the inverse problem would take the form of a spatiotemporal deconvolution. Further validation against nonlinear models, incorporation of additional background states, and comparison with existing estimation methods would be necessary steps to consider before applying the linearised model to estimate basal melt rates. We found that across-channel advection leads to diminished topography that could be difficult to associate with basal melting in the framework of an altimetry-based inverse method, although this issue could be circumvented with an alternative method if surface velocity data that resolves the flow response across the channel is available (Figure 8b).

Aside from non-hydrostatic effects, our analysis highlights several important aspects of channel stability and suggests that melt-rate estimates should be interpreted carefully in conjunction with strain rates and ice rheology. For example, previous work has suggested that a channel on the Dotson Ice Shelf, West Antarctica, will eventually break through the entire thickness of the ice column based on linearly extrapolating melt rate estimates [63]. Previous analysis and the simplified treatment herein shows that instability can arise when the timescale set by extensional thinning is faster than the intrinsic channel evolution timescale, which depends on the ice viscosity [47]. On the other hand, we found that channels can reach a stable steady state where melting is balanced by viscous flow towards the channel whenever melting is constant through time and extensional thinning is small, in agreement with recent numerical simulations [39]. Channel stability generally depends on the spectral properties of the melt rate when thinning rates are non-negligible (Figures 9-10). Thus, time-varying melt rates due to evolving ocean conditions or complex ice-ocean coupling such as melt enhancement along steep or rough basal surfaces also likely influences the stability of channels [15,64]. Careful consideration of the stress regime, ice rheology, and coupling with ocean physics is needed for predicting channel evolution and the potential for incision through the ice column.

We also found that across-channel advection leads to diminished topography (Figure 7b), especially at shorter wavelengths (Figure 8b). The topography is diminished because a portion of the melt rate is balanced by advection from the background flow rather than vertical deformation. These results suggest that channel development in the across-flow direction is hindered at short wavelengths, which could provide one explanation for why channels are preferentially oriented in the along-flow direction. The orientation of the ocean current or subglacial outflow that drives channel incision also influences the along-flow orientation as buoyant meltwater preferentially follows the ice-shelf profile towards the terminus [7,9]. However, these across-channel flow effects are negligible if the melting anomaly is advecting with the flow rather than stationary as in the examples shown in this study (Figure 7b and Figure 8b), which are akin to tectonic plate motion over a hot spot [55]. The melt rate can be expected to at least partially advect with the ice flow when localised melting involves entrainment of warmer waters in topographic features [9], whereas a stationary subglacial outflow plume could potentially produce advective effects similar to those highlighted here.

In our analysis, we assumed that the idealised ice shelf could be characterised by a simple reference state to focus on deviations from perfect flotation. Several nonlinear effects not considered in our analysis may also influence the evolution of melt-generated ice shelf topography. For example, ice deformation regimes such as proximity to the grounding line, varying ice-shelf geometry, fracture, buttressing, or viscoelasticity may produce different non-hydrostatic effects or stability criteria relative to the idealised shelves considered here [4,22,45,65]. Quantifying the influence of these more complex stress regimes on channel evolution would be valuable.

We have also assumed that the melting or freezing rate is a prescribed forcing function in this model. While considering non-hydrostatic effects can help to improve estimates of basal melting from surface observations, models that include oceanic physics coupled to ice deformation are needed to fully understand the physical processes governing ice-ocean interaction and predict the ice-shelf response to ocean warming [12,13,66–69]. Observations also suggest complex relations between ocean conditions, melting rate, and basal ice topography. For example, ice-penetrating radar and autonomous underwater vehicles have shown that melting depends on the ice roughness or slope of the ice-water interface [11,15,64]. Further modelling and analysis would be useful for elucidating the effects that these processes have on the evolution of ice-shelf topography that is generated by melting at the base.

In our linearised analysis, we excluded perturbations in ice-surface mass balance for simplicity. Localised changes in mass balance at the ice-shelf surface are often related to hydrology [70–74]. In particular, the drainage of ponded water on ice shelves can lead to flexure and potential instability [75–78]. For example, supraglacial lake drainage has been linked to the breakup of the Larsen B Ice Shelf [79,80]. As observations suggest that basal channels and surface hydrology can be coupled [81], implementing surface hydrology in ice-shelf models is a valuable avenue for future work [82,83]. While including surface mass balance perturbations in our linearised analysis is straightforward, we would need to modify our model so that the normal stress condition at the surface accounts for the load associated with ponded water and include additional physics to describe the redistribution of surface waters [84]. We could explore the effects of lateral variations in ice density due to variations in firn properties in a similar way [85]. We leave considerations of perturbations related to surface hydrology or ice density variations for future work.

Finally, the theory developed herein could potentially be extended to analyse the evolution of topography on icy satellites that are thought to have subsurface oceans, like Europa and Enceladus [86–88]. Our analysis diverges from previous treatments of icy satellite topography wherein pressure gradients are assumed to balance shear stresses similar to the shallow-ice approximation for land-based glaciers [89,90]. Further analysis of the physics governing topographic evolution on icy satellites and terrestrial ice shelves would be valuable for elucidating connections with thermomechanical processes at the ice-water interface [91,92].

6. Conclusions

Here, we have derived and analysed a linearised model for the evolution of ice-shelf topography that is generated by melting or freezing at the base. We presented a spectral decomposition of the linearised problem to elucidate the dominant modes and time scales governing channel evolution. The analysis shows that the flotation condition is the dominant mode at longer wavelengths, while shorter wavelength topography can persist in hydrostatic imbalance indefinitely. We illustrated through several examples the variety of topographic expressions that can result from a Gaussian-shaped melting anomaly when across-channel advection, extensional effects, and the width of the anomaly are modified. We validated the linearised approach for the examples herein by comparing steady solutions obtained via a Green's function to solutions of a fully nonlinear problem obtained with a finite element method. Future work should focus on including hydrostatic imbalance in basal melting estimates, further constraining the ice-ocean interactions that lead to channel incision, and determining the influence of channelisation on ice-shelf stability.

Data Accessibility. No new data are presented in this study. The code is openly available at https://www.doi.org/10.5281/zenodo.8171998 (DOI: 10.5281/zenodo.8171998).

Authors' Contributions. A.G.S. conceived the study, developed the analysis, conducted numerical simulations, and drafted the manuscript. C.R.M. and M.G.W. provided valuable insight in the analysis and helped revise the manuscript.

Competing Interests. The authors declare no competing interests.

Acknowledgements. We thank Jeremy Bassis and an anonymous reviewer for providing feedback that improved the presentation and scope of the manuscript. We also thank Jonathan Kingslake and David Porter for discussions about this work.

Funding. A.G.S. was supported by NSF (2012958). C.R.M. was supported by NSF (2012958); ARO (78811EG); and NASA (80NSSC21M0329).

Appendix A. Regularisation

To remove the singularities in R and B for the purpose of computation, we define the regularised relaxation and buoyancy functions

$$\mathsf{R}_\theta = (\theta + \mathsf{R}^{-1})^{-1}, \qquad \mathsf{B}_\theta = (\theta + \mathsf{B}^{-1})^{-1}, \tag{6.1}$$

where θ is a small regularisation parameter. We choose θ such that the analytical limit $\mathsf{R}_\theta - \mathsf{B}_\theta \to \frac{1}{4}$ as $k \to 0$ is attained at $k = 10^{-3}$, resulting in $\theta \approx 2.5 \times 10^{-14}$. The regularisation results in other analytical limits like the long-wavelength eigenvalue limit in (3.7) being respected at small k (Figure 3 and Figure 4). These regularisations are only used to facilitate computation of the solutions; we show in the main text that the solutions are well-defined. Analogous regularisations are employed for the velocity response functions derived in Appendix B and Appendix C. Further discussion of the physics behind the singularity and an alternative regularisation procedure that is motivated by a matched asymptotic analysis is presented in [47].

Appendix B. Vertical velocity

Velocity solutions can be obtained after solving for the elevations h and s. Here, we outline a derivation in the limit of no background extension ($\gamma = 0$). The surface elevation equations remedy the singularity of the system (2.29) in the limit $k \to 0$ by determining the long-wavelength component. In steady state, equations (2.11) and (2.12) imply that the long-wavelength limits of the vertical velocity at the surface and base are

$$\lim_{k\to 0} \widehat{w}|_{z=H} = 0, \qquad \lim_{k\to 0} \widehat{w}|_{z=0} = -\lim_{k\to 0} \widehat{m}. \tag{6.2}$$

The elevation solutions derived in the main text result in these limits being satisfied in (2.35) and (2.41). We apply the limits (6.2) to (2.25) to find that the the long-wavelength component of the vertical velocity on the interior of the ice is

$$\lim_{k\to 0} \widehat{w} = -\left(1 - \frac{z}{H}\right) \lim_{k\to 0} \widehat{m}. \tag{6.3}$$

The particular expression for $\widehat{w}$ (2.25) at an arbitrary depth is given by

$$\widehat{w} = -\mathsf{W}_h \widehat{h} - \mathsf{W}_s \delta \widehat{s}, \tag{6.4}$$

where the functions W_h and W_s are

$$\begin{aligned}
\mathsf{W}_h &= \frac{1}{t_\mathrm{r}}\Big[\Big(k'z'\left(\left(2k'+1\right)e^{2k'}-1\right)+k'+\left(k'+1\right)e^{2k'}- \\
&\quad \left(k'z'\left(2k'+e^{2k'}-1\right)-\left(k'+1\right)e^{2k'}-k'+1\right)e^{2k'z'}-1\Big)e^{k'(1-z')}\Big]/\mathsf{L} \qquad (6.5)\\
\mathsf{W}_s &= \frac{1}{t_\mathrm{r}}\Big[\Big(\left(k'z'\left(\left(2k'+1\right)e^{2k'}-1\right)-\left(2k'^2+2k'+1\right)e^{2k'}+1\right)e^{2k'z'} \\
&\quad -\left(k'z'\left(2k'+e^{2k'}-1\right)-2k'^2+2k'+e^{2k'}-1\right)e^{2k'}\Big)e^{-k'z'}\Big]/\mathsf{L} \qquad (6.6)\\
\mathsf{L} &= k'(e^{4k'}-2(1+2k'^2)e^{2k'}+1) \qquad (6.7)
\end{aligned}$$

These response functions reduce to R and B when evaluated at the upper and lower surfaces in accordance with equations (2.35) and (2.41).

Appendix C. Horizontal velocity

We now outline a derivation of expressions for the horizontal velocities. As before, we outline a derivation in the limit of no background extension ($\gamma = 0$). We derive only the component in the x direction, u; the derivation of the y component, v, is analogous except with k_x replaced by k_y. The transformed horizontal momentum equation (2.20) has the general solution

$$\widehat{u}(z) = \frac{ik_x}{2\bar{\eta}k}\left[e^{kz}\int_0^z \widehat{p}(\tilde{z})e^{-k\tilde{z}}\,\mathrm{d}\tilde{z} - e^{-kz}\int_0^z \widehat{p}(\tilde{z})e^{k\tilde{z}}\,\mathrm{d}\tilde{z}\right] + d_1 e^{kz} + d_2 e^{-kz}, \tag{6.8}$$

where d_1 and d_2 depend on k. Using the identity $\widehat{p} = \bar{\eta}\left(k^{-2}\widehat{w}_{zzz} - \widehat{w}_z\right)$, we find that equation (6.8) reduces to

$$\widehat{u}(z) = \frac{ik_x}{k^2}P(z) + d_1 e^{kz} + d_2 e^{-kz} \tag{6.9}$$

$$P(z) = \widehat{w}_z - \widehat{w}_z|_{z=0}\cosh(kz) - \frac{1}{k}\widehat{w}_{zz}|_{z=0}\sinh(kz). \tag{6.10}$$

Equation (6.9) and the vanishing shear-stress conditions, $\widehat{u}_z = -ik_x\widehat{w}$, at $z = H$ and $z = 0$ lead to the linear system

$$\begin{bmatrix} e^{k'} & -e^{-k'} \\ 1 & -1 \end{bmatrix}\begin{bmatrix} d_1 \\ d_2 \end{bmatrix} = -\frac{ik_x}{k^2}\begin{bmatrix} k\widehat{w}|_{z=H} + \frac{1}{k}P_z(H) \\ k\widehat{w}|_{z=0} \end{bmatrix}, \tag{6.11}$$

where $\widehat{w}|_{z=H}$ and $\widehat{w}|_{z=0}$ are given by (2.35) and (2.41), respectively. After solving the system (6.11) for the coefficients d_1 and d_2, we can write the horizontal velocity in (6.9) as

$$\widehat{u} = ik_x\left(\mathsf{U}_h\widehat{h} + \mathsf{U}_s\delta\widehat{s}\right), \tag{6.12}$$

where the response functions U_h and U_s are

$$\mathsf{U}_h = \frac{1}{t_\mathrm{r}}\left[z'((1-2k'-e^{2k'})e^{2k'z'}+1)+\left(1-z'(1+2k')\right)e^{2k'}+e^{2k'(z'+1)}(e^{2k'}-1)-1\right] \times e^{k'(1-z')}/\mathsf{L} \tag{6.13}$$

$$\mathsf{U}_s = \frac{1}{t_\mathrm{r}}\left[z'(e^{2k'z'}-e^{4k'}-(1+2k')e^{2k'(z'+1)})+2k'e^{2k'(z'+1)}+\left(-2k'z'+2k'+z'\right)e^{2k'}\right] \times e^{-k'z'}/\mathsf{L}, \tag{6.14}$$

where L is defined in (6.7). As with the vertical velocity, the coupling with the elevation solutions renders the horizontal velocity well-defined in the limit $k \to 0$ even though the system (6.11) is singular. We find that that $\widehat{u} \to 0$ as $k \to 0$ for the examples herein, which is the expected behavior for a symmetric flow field with vanishing horizontal integral.

References

1. Scambos TA, Bohlander J, Shuman CA, Skvarca P. 2004 Glacier acceleration and thinning after ice shelf collapse in the Larsen B embayment, Antarctica. *Geophysical Research Letters* **31**.
2. Paolo FS, Fricker HA, Padman L. 2015 Volume loss from Antarctic ice shelves is accelerating. *Science* **348**, 327–331.
3. Fürst JJ, Durand G, Gillet-Chaulet F, Tavard L, Rankl M, Braun M, Gagliardini O. 2016 The safety band of Antarctic ice shelves. *Nature Climate Change* **6**, 479–482.
4. Pegler SS. 2018 Marine ice sheet dynamics: the impacts of ice-shelf buttressing. *Journal of Fluid Mechanics* **857**, 605–647.
5. Rignot E, Steffen K. 2008 Channelized bottom melting and stability of floating ice shelves. *Geophysical Research Letters* **35**.
6. Joughin I, Alley RB. 2011 Stability of the West Antarctic ice sheet in a warming world. *Nature Geoscience* **4**, 506–513.
7. Alley KE, Scambos TA, Siegfried MR, Fricker HA. 2016 Impacts of warm water on Antarctic ice shelf stability through basal channel formation. *Nature Geoscience* **9**, 290–293.
8. Joughin I, Shapero D, Smith B, Dutrieux P, Barham M. 2021 Ice-shelf retreat drives recent Pine Island Glacier speedup. *Science Advances* **7**, eabg3080.
9. Alley KE, Scambos TA, Alley RB. 2023 The role of channelized basal melt in ice-shelf stability: recent progress and future priorities. *Annals of Glaciology* pp. 1–5.
10. Le Brocq AM, Ross N, Griggs JA, Bingham RG, Corr HF, Ferraccioli F, Jenkins A, Jordan TA, Payne AJ, Rippin DM et al.. 2013 Evidence from ice shelves for channelized meltwater flow beneath the Antarctic Ice Sheet. *Nature Geoscience* **6**, 945–948.
11. Dutrieux P, Stewart C, Jenkins A, Nicholls KW, Corr HF, Rignot E, Steffen K. 2014 Basal terraces on melting ice shelves. *Geophysical Research Letters* **41**, 5506–5513.
12. Gladish CV, Holland DM, Holland PR, Price SF. 2012 Ice-shelf basal channels in a coupled ice/ocean model. *Journal of Glaciology* **58**, 1227–1244.
13. Sergienko O. 2013 Basal channels on ice shelves. *Journal of Geophysical Research: Earth Surface* **118**, 1342–1355.
14. Langley K, Von Deschwanden A, Kohler J, Sinisalo A, Matsuoka K, Hattermann T, Humbert A, Nøst O, Isaksson E. 2014 Complex network of channels beneath an Antarctic ice shelf. *Geophysical Research Letters* **41**, 1209–1215.
15. Schmidt BE, Washam P, Davis PE, Nicholls KW, Holland DM, Lawrence JD, Riverman KL, Smith JA, Spears A, Dichek D et al.. 2023 Heterogeneous melting near the Thwaites Glacier grounding line. *Nature* **614**, 471–478.
16. Rignot E, Jacobs S, Mouginot J, Scheuchl B. 2013 Ice-shelf melting around Antarctica. *Science* **341**, 266–270.
17. Thomas RH. 1979 Ice shelves: a review. *Journal of Glaciology* **24**, 273–286.
18. Fricker HA, Popov S, Allison I, Young N. 2001 Distribution of marine ice beneath the Amery Ice Shelf. *Geophysical Research Letters* **28**, 2241–2244.
19. Joughin I, Padman L. 2003 Melting and freezing beneath Filchner-Ronne Ice Shelf, Antarctica. *Geophysical Research Letters* **30**.

20. Holland PR, Corr HF, Vaughan DG, Jenkins A, Skvarca P. 2009 Marine ice in Larsen ice shelf. *Geophysical Research Letters* **36**.
21. Galton-Fenzi B, Hunter J, Coleman R, Marsland S, Warner R. 2012 Modeling the basal melting and marine ice accretion of the Amery Ice Shelf. *Journal of Geophysical Research: Oceans* **117**.
22. Whiteford A, Horgan H, Leong W, Forbes M. 2022 Melting and refreezing in an ice shelf basal channel at the grounding line of the Kamb Ice Stream, West Antarctica. *Journal of Geophysical Research: Earth Surface* **127**, e2021JF006532.
23. Craven M, Allison I, Brand R, Elcheikh A, Hunter J, Hemer M, Donoghue S. 2004 Initial borehole results from the Amery Ice Shelf hot-water drilling project. *Annals of Glaciology* **39**, 531–539.
24. Craven M, Carsey F, Behar A, Matthews J, Brand R, Elcheikh A, Hall S, Treverrow A. 2005 Borehole imagery of meteoric and marine ice layers in the Amery Ice Shelf, East Antarctica. *Journal of Glaciology* **51**, 75–84.
25. Craven M, Allison I, Fricker HA, Warner R. 2009 Properties of a marine ice layer under the Amery Ice Shelf, East Antarctica. *Journal of Glaciology* **55**, 717–728.
26. Engelhardt H, Determann J. 1987 Borehole evidence for a thick layer of basal ice in the central Ronne Ice Shelf. *Nature* **327**, 318–319.
27. Oerter H, Kipfstuhl J, Determann J, Miller H, Wagenbach D, Minikin A, Graft W. 1992 Evidence for basal marine ice in the Filchner–Ronne Ice Shelf. *Nature* **358**, 399–401.
28. Treverrow A, Warner RC, Budd WF, Craven M. 2010 Meteoric and marine ice crystal orientation fabrics from the Amery Ice Shelf, East Antarctica. *Journal of Glaciology* **56**, 877–890.
29. Jansen D, Luckman A, Kulessa B, Holland PR, King EC. 2013 Marine ice formation in a suture zone on the Larsen C Ice Shelf and its influence on ice shelf dynamics. *Journal of Geophysical Research: Earth Surface* **118**, 1628–1640.
30. Kulessa B, Jansen D, Luckman AJ, King EC, Sammonds PR. 2014 Marine ice regulates the future stability of a large Antarctic ice shelf. *Nature communications* **5**, 3707.
31. McGrath D, Steffen K, Holland PR, Scambos T, Rajaram H, Abdalati W, Rignot E. 2014 The structure and effect of suture zones in the Larsen C Ice Shelf, Antarctica. *Journal of Geophysical Research: Earth Surface* **119**, 588–602.
32. Kulessa B, Booth AD, O'Leary M, McGrath D, King EC, Luckman AJ, Holland PR, Jansen D, Bevan SL, Thompson SS et al.. 2019 Seawater softening of suture zones inhibits fracture propagation in Antarctic ice shelves. *Nature Communications* **10**, 5491.
33. Larour E, Rignot E, Poinelli M, Scheuchl B. 2021 Physical processes controlling the rifting of Larsen C Ice Shelf, Antarctica, prior to the calving of iceberg A68. *Proceedings of the National Academy of Sciences* **118**, e2105080118.
34. Glen JW. 1955 The creep of polycrystalline ice. *Proceedings of the Royal Society of London. Series A. Mathematical and Physical Sciences* **228**, 519–538.
35. Greve R, Blatter H. 2009 *Dynamics of ice sheets and glaciers*. Springer Science & Business Media.
36. Cuffey KM, Paterson WSB. 2010 *The physics of glaciers*. Academic Press.
37. Van Der Veen CJ, Whillans I. 1989 Force budget: I. Theory and numerical methods. *Journal of Glaciology* **35**, 53–60.
38. Drews R. 2015 Evolution of ice-shelf channels in Antarctic ice shelves. *The Cryosphere* **9**, 1169–1181.
39. Wearing M, Stevens L, Dutrieux P, Kingslake J. 2021 Ice-shelf basal melt channels stabilized by secondary flow. *Geophysical Research Letters* **48**, e2021GL094872.
40. Chartrand A, Howat I. 2020 Basal channel evolution on the Getz Ice Shelf, West Antarctica. *Journal of Geophysical Research: Earth Surface* **125**, e2019JF005293.
41. Millgate T, Holland PR, Jenkins A, Johnson HL. 2013 The effect of basal channels on oceanic ice-shelf melting. *Journal of Geophysical Research: Oceans* **118**, 6951–6964.
42. Sergienko O, Goldberg D, Little C. 2013 Alternative ice shelf equilibria determined by ocean environment. *Journal of Geophysical Research: Earth Surface* **118**, 970–981.
43. Dallaston M, Hewitt I, Wells A. 2015 Channelization of plumes beneath ice shelves. *Journal of Fluid Mechanics* **785**, 109–134.
44. Humbert A, Steinhage D, Helm V, Hoerz S, Berendt J, Leipprand E, Christmann J, Plate C, Müller R. 2015 On the link between surface and basal structures of the Jelbart Ice Shelf, Antarctica. *Journal of Glaciology* **61**, 975–986.
45. Humbert A, Christmann J, Corr HF, Helm V, Höyns LS, Hofstede C, Müller R, Neckel N, Nicholls KW, Schultz T et al.. 2022 On the evolution of an ice shelf melt channel at the base of Filchner Ice Shelf, from observations and viscoelastic modeling. *The Cryosphere* **16**, 4107–4139.

46. Drews R, Schannwell C, Ehlers T, Gladstone R, Pattyn F, Matsuoka K. 2020 Atmospheric and oceanographic signatures in the ice shelf channel morphology of Roi Baudouin Ice Shelf, East Antarctica, inferred from radar data. *Journal of Geophysical Research: Earth Surface* **125**, e2020JF005587.
47. Bassis JN, Ma Y. 2015 Evolution of basal crevasses links ice shelf stability to ocean forcing. *Earth and Planetary Science Letters* **409**, 203–211.
48. Kachuck SB, Whitcomb M, Bassis JN, Martin DF, Price SF. 2022 Simulating ice-shelf extent using damage mechanics. *Journal of Glaciology* **68**, 987–998.
49. Zuber M, Parmentier E. 1986 Lithospheric necking: a dynamic model for rift morphology. *Earth and Planetary Science Letters* **77**, 373–383.
50. Fletcher RC. 1995 Three-dimensional folding and necking of a power-law layer: are folds cylindrical, and, if so, do we understand why?. *Tectonophysics* **247**, 65–83.
51. Budd W. 1970 Ice flow over bedrock perturbations. *Journal of Glaciology* **9**, 29–48.
52. Hutter K, Legerer F, Spring U. 1981 First-order stresses and deformations in glaciers and ice sheets. *Journal of Glaciology* **27**, 227–270.
53. Balise MJ, Raymond CF. 1985 Transfer of basal sliding variations to the surface of a linearly viscous glacier. *Journal of Glaciology* **31**, 308–318.
54. Gudmundsson GH. 2003 Transmission of basal variability to a glacier surface. *Journal of Geophysical Research: Solid Earth* **108**.
55. Turcotte DL, Schubert G. 2002 *Geodynamics*. Cambridge university press.
56. Stubblefield A, Creyts T, Kingslake J, Siegfried M, Spiegelman M. 2021 Surface expression and apparent timing of subglacial lake oscillations controlled by viscous ice flow. *Geophysical Research Letters* **48**, e2021GL094658.
57. Pegler SS, Worster MG. 2012 Dynamics of a viscous layer flowing radially over an inviscid ocean. *Journal of Fluid Mechanics* **696**, 152–174.
58. Stubblefield AG, Spiegelman M, Creyts TT. 2021 Variational formulation of marine ice-sheet and subglacial-lake grounding-line dynamics. *Journal of Fluid Mechanics* **919**, A23.
59. Millstein JD, Minchew BM, Pegler SS. 2022 Ice viscosity is more sensitive to stress than commonly assumed. *Communications Earth & Environment* **3**, 57.
60. Alnæs MS, Logg A, Ølgaard KB, Rognes ME, Wells GN. 2014 Unified Form Language: A Domain-Specific Language for Weak Formulations of Partial Differential Equations. *ACM Trans. Math. Softw.* **40**. (10.1145/2566630)
61. Scroggs MW, Dokken JS, Richardson CN, Wells GN. 2022a Construction of Arbitrary Order Finite Element Degree-of-Freedom Maps on Polygonal and Polyhedral Cell Meshes. *ACM Trans. Math. Softw.* **48**. (10.1145/3524456)
62. Scroggs MW, Baratta IA, Richardson CN, Wells GN. 2022b Basix: a runtime finite element basis evaluation library. *Journal of Open Source Software* **7**, 3982. (10.21105/joss.03982)
63. Gourmelen N, Goldberg DN, Snow K, Henley SF, Bingham RG, Kimura S, Hogg AE, Shepherd A, Mouginot J, Lenaerts JT et al.. 2017 Channelized melting drives thinning under a rapidly melting Antarctic ice shelf. *Geophysical Research Letters* **44**, 9796–9804.
64. Watkins RH, Bassis JN, Thouless M. 2021 Roughness of ice shelves is correlated with basal melt rates. *Geophysical Research Letters* **48**, e2021GL094743.
65. Marsh OJ, Fricker HA, Siegfried MR, Christianson K, Nicholls KW, Corr HF, Catania G. 2016 High basal melting forming a channel at the grounding line of Ross Ice Shelf, Antarctica. *Geophysical Research Letters* **43**, 250–255.
66. Mueller R, Padman L, Dinniman MS, Erofeeva S, Fricker HA, King M. 2012 Impact of tide-topography interactions on basal melting of Larsen C Ice Shelf, Antarctica. *Journal of Geophysical Research: Oceans* **117**.
67. Washam P, Nicholls KW, Münchow A, Padman L. 2020 Tidal modulation of buoyant flow and basal melt beneath Petermann Gletscher Ice Shelf, Greenland. *Journal of Geophysical Research: Oceans* **125**, e2020JC016427.
68. Bradley AT, Rosie Williams C, Jenkins A, Arthern R. 2022 Asymptotic analysis of subglacial plumes in stratified environments. *Proceedings of the Royal Society A* **478**, 20210846.
69. Richter O, Gwyther DE, King MA, Galton-Fenzi BK. 2022 The impact of tides on Antarctic ice shelf melting. *The Cryosphere* **16**, 1409–1429.
70. Bell RE, Chu W, Kingslake J, Das I, Tedesco M, Tinto KJ, Zappa CJ, Frezzotti M, Boghosian A, Lee WS. 2017 Antarctic ice shelf potentially stabilized by export of meltwater in surface river. *Nature* **544**, 344–348.

71. Kingslake J, Ely JC, Das I, Bell RE. 2017 Widespread movement of meltwater onto and across Antarctic ice shelves. *Nature* **544**, 349–352.
72. Bell RE, Banwell AF, Trusel LD, Kingslake J. 2018 Antarctic surface hydrology and impacts on ice-sheet mass balance. *Nature Climate Change* **8**, 1044–1052.
73. MacDonald GJ, Banwell AF, Willis IC, Mayer DP, Goodsell B, MacAYEAL DR. 2019 Formation of pedestalled, relict lakes on the McMurdo Ice Shelf, Antarctica. *Journal of Glaciology* **65**, 337–343.
74. Spergel JJ, Kingslake J, Creyts T, van Wessem M, Fricker HA. 2021 Surface meltwater drainage and ponding on Amery Ice Shelf, East Antarctica, 1973–2019. *Journal of Glaciology* **67**, 985–998.
75. Banwell AF, Macayeal DR. 2015 Ice-shelf fracture due to viscoelastic flexure stress induced by fill/drain cycles of supraglacial lakes. *Antarctic Science* **27**, 587–597.
76. MacAYEAL DR, Sergienko OV, Banwell AF. 2015 A model of viscoelastic ice-shelf flexure. *Journal of Glaciology* **61**, 635–645.
77. Banwell AF, Willis IC, Macdonald GJ, Goodsell B, MacAyeal DR. 2019 Direct measurements of ice-shelf flexure caused by surface meltwater ponding and drainage. *Nature communications* **10**, 730.
78. Arthur JF, Stokes CR, Jamieson SS, Carr JR, Leeson AA. 2020 Distribution and seasonal evolution of supraglacial lakes on Shackleton Ice Shelf, East Antarctica. *The Cryosphere* **14**, 4103–4120.
79. Banwell AF, MacAyeal DR, Sergienko OV. 2013 Breakup of the Larsen B Ice Shelf triggered by chain reaction drainage of supraglacial lakes. *Geophysical Research Letters* **40**, 5872–5876.
80. Leeson A, Forster E, Rice A, Gourmelen N, Van Wessem J. 2020 Evolution of supraglacial lakes on the Larsen B ice shelf in the decades before it collapsed. *Geophysical Research Letters* **47**, e2019GL085591.
81. Dow CF, Lee WS, Greenbaum JS, Greene CA, Blankenship DD, Poinar K, Forrest AL, Young DA, Zappa CJ. 2018 Basal channels drive active surface hydrology and transverse ice shelf fracture. *Science Advances* **4**, eaao7212.
82. Buzzard S, Feltham D, Flocco D. 2018a A mathematical model of melt lake development on an ice shelf. *Journal of Advances in Modeling Earth Systems* **10**, 262–283.
83. Buzzard S, Feltham D, Flocco D. 2018b Modelling the fate of surface melt on the Larsen C Ice Shelf. *The Cryosphere* **12**, 3565–3575.
84. Schoof C, Cook S, Kulessa B, Thompson S. 2023 The drainage of glacier and ice sheet surface lakes. *Journal of Fluid Mechanics* **961**, A4.
85. Holland PR, Corr HF, Pritchard HD, Vaughan DG, Arthern RJ, Jenkins A, Tedesco M. 2011 The air content of Larsen ice shelf. *Geophysical Research Letters* **38**.
86. Carr MH, Belton MJ, Chapman CR, Davies ME, Geissler P, Greenberg R, McEwen AS, Tufts BR, Greeley R, Sullivan R et al.. 1998 Evidence for a subsurface ocean on Europa. *Nature* **391**, 363–365.
87. Pappalardo RT, Belton MJ, Breneman H, Carr M, Chapman CR, Collins G, Denk T, Fagents S, Geissler PE, Giese B et al.. 1999 Does Europa have a subsurface ocean? Evaluation of the geological evidence. *Journal of Geophysical Research: Planets* **104**, 24015–24055.
88. Nimmo F, Pappalardo RT. 2016 Ocean worlds in the outer solar system. *Journal of Geophysical Research: Planets* **121**, 1378–1399.
89. Nye JF. 1952 The mechanics of glacier flow. *Journal of Glaciology* **2**, 82–93.
90. Nimmo F. 2004 Non-Newtonian topographic relaxation on Europa. *Icarus* **168**, 205–208.
91. Buffo J, Schmidt B, Huber C, Meyer C. 2021a Characterizing the ice-ocean interface of icy worlds: A theoretical approach. *Icarus* **360**, 114318.
92. Buffo J, Meyer C, Parkinson J. 2021b Dynamics of a solidifying icy satellite shell. *Journal of Geophysical Research: Planets* **126**, e2020JE006741.